which was accelerated from 4 to 40 rpm over a 300-second period and kept at the top speed for more than 100 seconds each day for 3 consecutive days. On the third day, latency to fall from the rotarod was measured as a baseline performance. On the seventh day after implantation of the minipump, mice were tested on the rotarod, and latency to fall off was measured after 3-NP treatment.

Antibodies. The primary antibodies used were mouse monoclonal anti-8-oxo-dG (N45.1, JaICa, Fukuroi); rabbit anti-DARPP32 (Cell Signaling Technology); mouse anti-DARPP32 (BD Transduction Laboratories); rat anti-F4/80 (Oxford); goat anti-TFAM (Santa Cruz Biotechnology Inc.); mouse anti-α–spectrin (Chemicon); mouse anti-AIF (Santa Cruz Biotechnology Inc.); mouse anti-PAR (Trevigen), rabbit anti-ssDNA (Immuno-Biological Laboratories), rabbit anti-calbindin D-28K (Chemicon); rabbit anti-GFAP (Dako); rabbit anti-Hsp60 (Abcam); rabbit anti-OGG1, which recognizes the conserved region of human OGG1 proteins (52); rabbit anti-MTH1 (NB100-109, Novus Biologicals); and rabbit anti-MUTYH, which was raised against recombinant human MUTYH (53). The ssDNA antibody recognizes single-stranded regions of DNA with a length of at least 6 deoxynucleotides, which can be generated by SSBs or DSBs with resection of the ends (45, 54).

Immunohistochemistry. Tissue preparation and immunohistochemical analyses were performed as described previously (31). Brains were cut on a cryostat at a thickness of 40 μm and collected as free-floating sections in PBS; these were then processed immediately for immunohistochemistry (IHC). Free-floating sections were subjected to appropriate pretreatment and reaction with a primary antibody and then processed using a Vector ABC kit (Vector Laboratories) with the proper biotinylated secondary antibody. Then, the 3,3′-diaminobenzidine (DAB)/nickel (Vector Laboratories) reaction was used to visualize the bound secondary antibody. Some sections were counterstained with cresyl violet. Digital images were acquired using an Axioskop2 Plus microscope, equipped with an AxioCam CCD camera, and Axiovision 3.1 imaging software (Carl Zeiss Inc.) was used.

Laser-scanning confocal immunofluorescent microscopy. Free-floating sections incubated with the appropriate primary antibody were then further incubated with a proper Alexa Fluor–labeled secondary antibody (Invitrogen) in a solution containing DAPI (0.05 μg/ml, Sigma-Aldrich). Confocal images were acquired using a confocal laser microscopy system (LSM 510META-V3.2 software; Carl Zeiss Inc.) attached to an inverted microscope (Axiovert 200M). Images of the immunostained sections were taken within 48 hours.

Quantitative immunodetection of 8-oxoG. For immunodetection of 8-oxoG in nDNA or mtDNA, free-floating sections were pretreated as described previously (31, 32). Briefly, to detect 8-oxoG in the mtDNA, sections were pretreated only with RNase (5 mg/ml; Sigma-Aldrich) and were directly subjected to IHC with the anti-8-oxo-dG antibody. To detect 8-oxoG in nDNA, RNase-treated sections were further pretreated with 2N HCl to denature the nDNA, thus enabling the antibody to access 8-oxoG in nDNA. These pretreated sections were subjected to IHC with the anti-8-oxo-dG antibody. The intensity of 8-oxoG IR in the whole striatum was measured in each digital image using ImageJ 1.42 (NIH). Pretreated sections reacted with the anti-8-oxo-dG as described above were also subjected to immunofluorescence microscopy with a proper Alexa Fluor–labeled secondary antibody. The mitochondrial 8-oxo-dG index in a single neuron was measured in each laser confocal image of the immunofluorescence samples using ImageJ. Twenty neurons were measured to obtain the mean mitochondrial 8-oxo-dG index for each animal.

Quantification of the level of nuclear 8-oxo-dG in striatum by LC-MS/MS. Ten-week-old male WT and *Mth1/Ogg1*-DKO were subjected to PBS or 3-NP administration. The mice were euthanized by cervical dislocation, and the striata were immediately removed and frozen in liquid nitrogen. The tissues were stored at -80°C and analyzed within 7 days of collection. No difference in the level of 8-oxo-dG was observed between tissues stored at -80°C and freshly isolated tissues. DNA was extracted from striata using the DNA Extractor TIS Kit (No. 296-67701, Wako) as described in the instructions for the kit, with a few modifications: 10 mM 2, 2, 6, 6-tetramethylpiperidine-N-oxyl (TEMPO, Wako) and 100 μM 2′-deoxycoformycin, an adenosine deaminase inhibitor provided by the Chemo-Sero-Therapeutic Research Institute (Kumamoto, Japan), were added to all reagents at all stages of manipulation. To allow for accurate quantitation of 8-oxo-dG and to account for the signal variability of the mass spectrometer, [^{15}N5]-labeled 8-oxo-dG (NLM-6715-0, Cambridge Isotope Laboratories Inc.) was added as a stable isotope internal standard prior to enzymatic hydrolysis of the DNA samples. The stable internal standards [^{15}N5] 8-oxo-dG, sodium acetate buffer (ABI, #400884, pH 4.5), nuclease P1 (Yamas), and acid phosphatase (P-0157; Sigma-Aldrich) were added to the DNA samples; samples were then transferred to filter tubes (Ultrafree-MC probind 0.45 μm; Millipore), and centrifuged at 12,000 *g* for 3 minutes. The digested samples were subjected to LC-MS/MS analysis using a Shimadzu VP-10 HPLC system connected to an API3000 MS/MS system (PE-SCIEX), and the ratios of 8-oxo-dG to 10^6 dG in the samples were determined as described previously (55).

Histochemical detection of mitochondrial cytochrome c oxidase activity. For detection of mitochondrial cytochrome *c* oxidase activity in frozen sections, brain sections (thickness, 40 μm) were prepared from WT and *Mutyh*-KO mice administered PBS or 3-NP (150 mg/kg/d) for 7 days. Brain sections were incubated for 3 hours at 37°C in a solution containing cytochrome *c* (0.3 mg/ml), DAB (0.5 mg/ml), and sucrose (40 mg/ml) in PBS. Then sections washed in PBS were dehydrated with ethanol, immersed in xylene and mounted on slide glass, and digital images were acquired. The intensity of DAB staining cytochrome *c* oxidase activity in the whole striatum was measured in each digital image using ImageJ 1.42.

Morphometric analysis. The densities of neurons and glial cells in the dorsolateral striatum (bregma, 0.86 mm to approximately 0.62 mm) (56) were estimated by counting those on cresyl violet–stained sections. Neurons were identified as large cells with typical morphological features including a round, oval, or polygonal shape, and glial cells were identified as cells with profiles distinguished by their small, round, and hyperchromatic nuclei. The density of MSNs in the dorsolateral striatum was estimated by counting DARPP32-positive cells.

Western blot analysis. Striata were isolated from *Mth1/Ogg1*-DKO or WT mice on the fourth and seventh days of exposure to 3-NP or on the seventh day of exposure to PBS. Mouse striata were homogenized in ice-cold lysis buffer containing 50 mM Tris-HCl, pH 8.0, 150 mM NaCl, 1.0% NP-40, 0.5% sodium deoxycholate, 0.1% SDS, and protease inhibitor mixture (Nacalai Tesque). The homogenates were then centrifuged at 89,000 *g* for 30 minutes at 4°C, and the supernatants were collected. Western blot analysis was performed according to previously described methods (57, 58). Protein concentration in the supernatant was measured using a DC protein assay kit (Bio-Rad). Equal amounts of total protein (5 μg) were separated by SDS-PAGE. Anti-α-spectrin (1:10,000), anti-AIF (1:500), and anti-β-actin (1:10,000) antibodies were used. The intensity of each band was quantified using an LAS1000 image analyzer and Image Gauge, version 3.2 software (Fujifilm).

Electron microscopy. For transmission electron microscopy, mouse brains were prefixed with 4% paraformaldehyde and 2.5% glutaraldehyde (TAAB Laboratories), washed with a cacodylate buffer, postfixed in osmium tetroxide (Nacalai Tesque), dehydrated in ascending concentrations of alcohol and uranyl acetate (MERCK), and embedded in epoxy resin (TAAB 812 resin. TAAB Laboratories). Ultrathin sections (100 nm) were cut, and examined under a transmission electron microscope (Tecnai 20; FEI Corp.). For electron microscopic immunocytochemistry to detect MUTYH

protein, fixed mouse brains were incubated in 2.3 M sucrose and then in 20% polyvinylpyrrolidone (Nacalai Tesque) prepared in 1.8 M sucrose. Ultrathin sections (100 nm) were cut, blocked in 3% BSA, incubated with rabbit anti-MUTYH antibody, then with a secondary antibody, anti-rabbit IgG-gold (10 nm; EY Lab.). Sections were post-fixed with 2.5% glutaraldehyde in 0.1 M cacodylate buffer, mounted with 0.1% uranyl acetate in 2% polyvinyl alcohol (Sigma-Aldrich), and examined under transmission electron microscope.

Statistics. Statistical analyses were conducted using JMP 9.02 (SAS Institute Inc.). Data are presented as least square (LS) means ± SEM. To assess statistical significance, we performed 1-way ANOVA for effects of treatment or 2-way ANOVA with interaction for effects of genotype and treatment, and interactions between genotype and treatment; results obtained by standard LS fits are shown. For multiple comparison tests, 1-way ANOVA analyses were followed by a post hoc Hsu's MCB test, while 2-way ANOVA analyses were followed by a post hoc Tukey's HSD test. Student's *t* test was applied for individual pairwise comparisons in all cases. The threshold for statistical significance was $P < 0.05$.

Study approval. The handling and killing of all animals were done in accordance with national prescribed guidelines, and ethical approval for the studies was granted by the Animal Care and Use Committee of Kyushu University.

Acknowledgments

This work was supported by grants from the Ministry of Education, Culture, Sports, Science and Technology of Japan (20013034), the Japan Society for the Promotion of Science (18300124, 19390114, 22221004, 22501014), and the Kyushu University Global COE program (Cell-rate Decision Function and Dysfunction in Homeostasis). We thank Yasunari Sakai, Dongchon Kang, Mami Noda, and Mizuki Ohno for helpful discussions; Ryo Ugawa (Laboratory for Technical Support, Medical Institute of Bioregulation, Kyushu University, Kyushu, Japan) for electron microscopy; and Setsuko Kitamura, Noami Adachi, Kazumi Asakawa, and Kaoru Nakabeppu for their technical assistance.

Received for publication May 29, 2012, and accepted in revised form September 13, 2012.

Address correspondence to: Yusaku Nakabeppu, Kyushu University, Division of Neurofunctional Genomics, Department of Immunobiology and Neuroscience, Medical Institute of Bioregulation, Kyushu University, 3-1-1 Maidashi, Higashi-ku, Fukuoka, 812-8582, Japan. Phone: 81.92.642.6800; Fax: 81.92.642.6791; E-mail: yusaku@bioreg.kyushu-u.ac.jp.

1. Ames BN, Shigenaga MK, Hagen TM. Oxidants, antioxidants, and the degenerative diseases of aging. *Proc Natl Acad Sci U S A.* 1993;90(17):7915–7922.
2. Finkel T, Holbrook NJ. Oxidants, oxidative stress and the biology of ageing. *Nature.* 2000; 408(6809):239–247.
3. Maynard S, Schurman SH, Harboe C, de Souza-Pinto NC, Bohr VA. Base excision repair of oxidative DNA damage and association with cancer and aging. *Carcinogenesis.* 2009;30(1):2–10.
4. Nakabeppu Y, Sakumi K, Sakamoto K, Tsuchimoto D, Tsuzuki T, Nakatsu Y. Mutagenesis and carcinogenesis caused by the oxidation of nucleic acids. *Biol Chem.* 2006;387(4):373–379.
5. Foti JJ, Devadoss B, Winkler JA, Collins JJ, Walker GC. Oxidation of the guanine nucleotide pool underlies cell death by bactericidal antibiotics. *Science.* 2012;336(6079):315–319.
6. Kasai H. Chemistry-based studies on oxidative DNA damage: formation, repair, and mutagenesis. *Free Radic Biol Med.* 2002;33(4):450–456.
7. Kasai H, Nishimura S. Hydroxylation of deoxyguanosine at the C-8 position by ascorbic acid and other reducing agents. *Nucleic Acids Res.* 1984; 12(4):2137–2145.
8. Sakumi K, et al. Cloning and expression of cDNA for a human enzyme that hydrolyzes 8-oxo-dGTP, a mutagenic substrate for DNA synthesis. *J Biol Chem.* 1993;268(31):23524–23530.
9. Furuichi M, et al. Genomic structure and chromosome location of the human mutT homologue gene *MTH1* encoding 8-oxo-dGTPase for prevention of A:T to C:G transversion. *Genomics.* 1994; 24(3):485–490.
10. Aburatani H, et al. Cloning and characterization of mammalian 8-hydroxyguanine-specific DNA glycosylase/apurinic, apyrimidinic lyase, a functional mutM homologue. *Cancer Res.* 1997; 57(11):2151–2156.
11. Slupska MM, Baikalov C, Luther WM, Chiang JH, Wei YF, Miller JH. Cloning and sequencing a human homolog (*hMYH*) of the *Escherichia coli mutY* gene whose function is required for the repair of oxidative DNA damage. *J Bacteriol.* 1996; 178(13):3885–3892.
12. Tsuzuki T, et al. Spontaneous tumorigenesis in mice defective in the *MTH1* gene encoding 8-oxo-dGTPase. *Proc Natl Acad Sci U S A.* 2001; 98(20):11456–11461.
13. Sakumi K, et al. *Ogg1* knockout-associated lung tumorigenesis and its suppression by Mth1 gene disruption. *Cancer Res.* 2003;63(5):902–905.
14. Sakamoto K, et al. MUTYH-null mice are susceptible to spontaneous and oxidative stress induced intestinal tumorigenesis. *Cancer Res.* 2007; 67(14):6599–6604.
15. Xie Y, et al. Deficiencies in mouse *Myh* and *Ogg1* result in tumor predisposition and G to T mutations in codon 12 of the *K-ras* oncogene in lung tumors. *Cancer Res.* 2004;64(9):3096–3102.
16. Shimura-Miura H, Hattori N, Kang D, Miyako K, Nakabeppu Y, Mizuno Y. Increased 8-oxo-dGTPase in the mitochondria of substantia nigral neurons in Parkinson's disease. *Ann Neurol.* 1999;46(6):920–924.
17. Wang J, Xiong S, Xie C, Markesbery WR, Lovell MA. Increased oxidative damage in nuclear and mitochondrial DNA in Alzheimer's disease. *J Neurochem.* 2005;93(4):953–962.
18. Polidori MC, Mecocci P, Browne SE, Senin U, Beal MF. Oxidative damage to mitochondrial DNA in Huntington's disease parietal cortex. *Neurosci Lett.* 1999;272(1):53–56.
19. Fukae J, et al. Expression of 8-oxoguanine DNA glycosylase (OGG1) in Parkinson's disease and related neurodegenerative disorders. *Acta Neuropathol.* 2005; 109(3):256–262.
20. Furuta A, Iida T, Nakabeppu Y, Iwaki T. Expression of hMTH1 in the hippocampi of control and Alzheimer's disease. *Neuroreport.* 2001;12(13):2895–2899.
21. Arai T, et al. Up-regulation of hMUTYH, a DNA repair enzyme, in the mitochondria of substantia nigra in Parkinson's disease. *Acta Neuropathol.* 2006; 112(2):139–145.
22. Iida T, Furuta A, Nishioka K, Nakabeppu Y, Iwaki T. Expression of 8-oxoguanine DNA glycosylase is reduced and associated with neurofibrillary tangles in Alzheimer's disease brain. *Acta Neuropathol.* 2002; 103(1):20–25.
23. Parent A. Extrinsic connections of the basal ganglia. *Trends Neurosci.* 1990;13(7):254–258.
24. Gould DH, Gustine DL. Basal ganglia degeneration, myelin alterations, and enzyme inhibition induced in mice by the plant toxin 3-nitropropanoic acid. *Neuropathol Appl Neurobiol.* 1982;8(5):377–393.
25. Brouillet E, et al. Chronic mitochondrial energy impairment produces selective striatal degeneration and abnormal choreiform movements in primates. *Proc Natl Acad Sci U S A.* 1995;92(15):7105–7109.
26. Brouillet E, Conde F, Beal MF, Hantraye P. Replicating Huntington's disease phenotype in experimental animals. *Prog Neurobiol.* 1999;59(5):427–468.
27. De Luca G, et al. A role for oxidized DNA precursors in Huntington's disease-like striatal neurodegeneration. *PLoS Genet.* 2008;4(11):e1000266.
28. Nakabeppu Y, Oka S, Sheng Z, Tsuchimoto D, Sakumi K. Programmed cell death triggered by nucleotide pool damage and its prevention by MutT homolog-1 (MTH1) with oxidized purine nucleoside triphosphatase. *Mutat Res.* 2010; 703(1):51–58.
29. Guyot MC, Hantraye P, Dolan R, Palfi S, Maziere M, Brouillet E. Quantifiable bradykinesia, gait abnormalities and Huntington's disease-like striatal lesions in rats chronically treated with 3-nitropropionic acid. *Neuroscience.* 1997;79(1):45–56.
30. Ludolph AC, He F, Spencer PS, Hammerstad J, Sabri M. 3-Nitropropionic acid-exogenous animal neurotoxin and possible human striatal toxin. *Can J Neurol Sci.* 1991;18(4):492–498.
31. Yamaguchi H, et al. MTH1, an oxidized purine nucleoside triphosphatase, protects the dopamine neurons from oxidative damage in nucleic acids caused by 1-methyl-4-phenyl-1,2,3,6-tetrahydropyridine. *Cell Death Differ.* 2006;13(4):551–563.
32. Ohno M, Oka S, Nakabeppu Y. Quantitative analysis of oxidized guanine, 8-oxoguanine, in mitochondrial DNA by immunofluorescence method. *Methods Mol Biol.* 2009;554:199–212.
33. Alam TI, et al. Human mitochondrial DNA is packaged with TFAM. *Nucleic Acids Res.* 2003; 31(6):1640–1645.
34. Oka S, Ohno M, Tsuchimoto D, Sakumi K, Furuichi M, Nakabeppu Y. Two distinct pathways of cell death triggered by oxidative damage to nuclear and mitochondrial DNAs. *EMBO J.* 2008; 27(2):421–432.
35. Czogalla A, Sikorski AF. Spectrin and calpain: a 'target' and a 'sniper' in the pathology of neuronal cells. *Cell Mol Life Sci.* 2005;62(17):1913–1924.
36. Brouillet E, Jacquard C, Bizat N, Blum D. 3-Nitropropionic acid: a mitochondrial toxin to uncover physiopathological mechanisms underlying striatal degeneration in Huntington's disease. *J Neurochem.* 2005;95(6):1521–1540.

37. Geddes JW, Bondada V, Tekirian TL, Pang Z, Siman RG. Perikaryal accumulation and proteolysis of neurofilament proteins in the post-mortem rat brain. *Neurobiol Aging.* 1995;16(4):651–660.
38. Hong SJ, Dawson TM, Dawson VL. Nuclear and mitochondrial conversations in cell death: PARP-1 and AIF signaling. *Trends Pharmacol Sci.* 2004; 25(5):259–264.
39. Ullrich O, Diestel A, Eyüpoglu IY, Nitsch R. Regulation of microglial expression of integrins by poly(ADP-ribose) polymerase-1. *Nat Cell Biol.* 2001; 3(12):1035–1042.
40. Ichikawa J, et al. Oxidation of mitochondrial deoxynucleotide pools by exposure to sodium nitroprusside induces cell death. *DNA Repair.* 2008; 7(3):418–430.
41. Oka S, Nakabeppu Y. DNA glycosylase encoded by *MUTYH* functions as a molecular switch for programmed cell death under oxidative stress to suppress tumorigenesis. *Cancer Sci.* 2011;102(4):677–682.
42. Yoshimura D, et al. An oxidized purine nucleoside triphosphatase, MTH1, suppresses cell death caused by oxidative stress. *J Biol Chem.* 2003; 278(39):37965–37973.
43. Kajitani K, Yamaguchi H, Dan Y, Furuichi M, Kang D, Nakabeppu Y. MTH1, an oxidized purine nucleoside triphosphatase, suppresses the accumulation of oxidative damage of nucleic acids in the hippocampal microglia during kainate-induced excitotoxicity. *J Neurosci.* 2006;26(6):1688–1698.
44. Imam SZ, Karahalil B, Hogue BA, Souza-Pinto NC, Bohr VA. Mitochondrial and nuclear DNA-repair capacity of various brain regions in mouse is altered in an age-dependent manner. *Neurobiol Aging.* 2006;27(8):1129–1136.
45. Kawarada Y, Miura N, Sugiyama T. Antibody against single-stranded DNA useful for detecting apoptotic cells recognizes hexadeoxynucleotides with various base sequences. *J Biochem.* 1998;123(3):492–498.
46. Ryu JK, Nagai A, Kim J, Lee MC, McLarnon JG, Kim SU. Microglial activation and cell death induced by the mitochondrial toxin 3-nitropropionic acid: in vitro and in vivo studies. *Neurobiol Dis.* 2003; 12(2):121–132.
47. Lin MT, Beal MF. Mitochondrial dysfunction and oxidative stress in neurodegenerative diseases. *Nature.* 2006;443(7113):787–795.
48. Block ML, Zecca L, Hong JS. Microglia-mediated neurotoxicity: uncovering the molecular mechanisms. *Nat Rev Neurosci.* 2007;8(1):57–69.
49. Vosler PS, Brennan CS, Chen J. Calpain-mediated signaling mechanisms in neuronal injury and neurodegeneration. *Mol Neurobiol.* 2008;38(1):78–100.
50. Nakabeppu Y, Tsuchimoto D, Yamaguchi H, Sakumi K. Oxidative damage in nucleic acids and Parkinson's disease. *J Neurosci Res.* 2007;85(5):919–934.
51. Hirano S, et al. Mutator phenotype of MUTYH-null mouse embryonic stem cells. *J Biol Chem.* 2003; 278(40):38121–38124.
52. Nishioka K, et al. Expression and differential intracellular localization of two major forms of human 8-oxoguanine DNA glycosylase encoded by alternatively spliced *OGG1* mRNAs. *Mol Biol Cell.* 1999;10(5):1637–1652.
53. Ohtsubo T, et al. Identification of human MutY homolog (hMYH) as a repair enzyme for 2-hydroxyadenine in DNA and detection of multiple forms of hMYH located in nuclei and mitochondria. *Nucleic Acids Res.* 2000;28(6):1355–1364.
54. Naruse I, Keino H, Kawarada Y. Antibody against single-stranded DNA detects both programmed cell death and drug-induced apoptosis. *Histochemistry.* 1994;101(1):73–78.
55. Tsuruya K, et al. Accumulation of 8-oxoguanine in the cellular DNA and the alteration of the OGG1 expression during ischemia-reperfusion injury in the rat kidney. *DNA Repair.* 2003;2(2):211–229.
56. Franklin KBJ, Paxinos G. *The Mouse Brain In Stereotaxic Coordinates.* San Diego, California, USA: Academic Press; 1997.
57. Iyama T, Abolhassani N, Tsuchimoto D, Nonaka M, Nakabeppu Y. NUDT16 is a (deoxy)inosine diphosphatase, and its deficiency induces accumulation of single-strand breaks in nuclear DNA and growth arrest. *Nucleic Acids Res.* 2010;38(14):4834–4843.
58. Tsuchimoto D, et al. Human APE2 protein is mostly localized in the nuclei and to some extent in the mitochondria, while nuclear APE2 is partly associated with proliferating cell nuclear antigen. *Nucleic Acids Res.* 2001;29(11):2349–2360.

OPEN ACCESS Freely available online

PLOS ONE

8-Oxoguanine DNA Glycosylase (OGG1) Deficiency Increases Susceptibility to Obesity and Metabolic Dysfunction

Harini Sampath[1], Vladimir Vartanian[1], M. Rick Rollins[1], Kunihiko Sakumi[2], Yusaku Nakabeppu[2]*, R. Stephen Lloyd[1]*

1 Department of Molecular and Medical Genetics, Center for Research on Occupational and Environmental Toxicology, Oregon Health and Science University, Portland, Oregon, United States of America, **2** Division of Neurofunctional Genomics, Department of Immunobiology and Neuroscience, Medical Institute of Bioregulation, and Research Center for Nucleotide Pool, Kyushu University, Fukuoka, Japan

Abstract

Oxidative damage to DNA is mainly repaired via base excision repair, a pathway that is catalyzed by DNA glycosylases such as 8-oxoguanine DNA glycosylase (OGG1). While OGG1 has been implicated in maintaining genomic integrity and preventing tumorigenesis, we report a novel role for OGG1 in altering cellular and whole body energy homeostasis. OGG1-deficient (*Ogg1*$^{-/-}$) mice have increased adiposity and hepatic steatosis following exposure to a high-fat diet (HFD), compared to wild-type (WT) animals. *Ogg1*$^{-/-}$ animals also have higher plasma insulin levels and impaired glucose tolerance upon HFD feeding, relative to WT counterparts. Analysis of energy expenditure revealed that HFD-fed *Ogg1*$^{-/-}$ mice have a higher resting VCO_2 and consequently, an increased respiratory quotient during the resting phase, indicating a preference for carbohydrate metabolism over fat oxidation in these mice. Additionally, microarray and quantitative PCR analyses revealed that key genes of fatty acid oxidation, including carnitine palmitoyl transferase-1, and the integral transcriptional co-activator *Pgc-1α* were significantly downregulated in *Ogg1*$^{-/-}$ livers. Multiple genes involved in TCA cycle metabolism were also significantly reduced in livers of *Ogg1*$^{-/-}$ mice. Furthermore, hepatic glycogen stores were diminished, and fasting plasma ketones were significantly reduced in *Ogg1*$^{-/-}$ mice. Collectively, these data indicate that OGG1 deficiency alters cellular substrate metabolism, favoring a fat sparing phenotype, that results in increased susceptibility to obesity and related pathologies in *Ogg1*$^{-/-}$ mice.

Citation: Sampath H, Vartanian V, Rollins MR, Sakumi K, Nakabeppu Y, et al. (2012) 8-Oxoguanine DNA Glycosylase (OGG1) Deficiency Increases Susceptibility to Obesity and Metabolic Dysfunction. PLoS ONE 7(12): e51697. doi:10.1371/journal.pone.0051697

Editor: Ferenc Gallyas, University of Pecs Medical School, Hungary

Received August 30, 2012; **Accepted** November 5, 2012; **Published** December 17, 2012

Funding: This work was supported by American Heart Association Postdoctoral grant 11POST7480004 (HS) and National Institutes of Health (NIH) R01 DK075974 (RSL). The funders had no role in study design, data collection and analysis, decision to publish, or preparation of the manuscript.

Competing Interests: The authors have declared that no competing interests exist.

* E-mail: yusaku@bioreg.kyushu-u.ac.jp (YN); lloydst@ohsu.edu (RSL)

Introduction

If left unrepaired, oxidative damage to DNA from exogenous oxidants, as well as endogenous metabolic byproducts, can lead to cellular transformation and ultimately to the development of tumors. Non-bulky oxidative DNA lesions are mainly repaired via the base-excision repair (BER) pathway [1–3], which is initiated by DNA glycosylases, such as 8-oxoguanine DNA glycosylase (OGG1), Nei endonuclease VIII-like (NEIL)1, NEIL2, NEIL3, and endonuclease III-like 1 (NTH1). These enzymes recognize and excise specific subsets of lesions, and in some cases, further process the damaged site to a single-strand break via their intrinsic apurinic/apyrimidinic lyase activity [2–4].

7,8-dihydro-8-oxoguanine (8-oxoG) is one of the most commonly formed oxidative lesions in the cell. Since it mispairs with A during replication, 8-oxoG is also a highly mutagenic lesion, producing G:C to T:A transversions. OGG1, a DNA repair glycosylase that localizes to both the nucleus and mitochondria, is the main enzyme responsible for identification and excision of 8-oxoG lesions [5–9]. OGG1 is hypothesized to play a role in several disease pathways, including various cancers [4,10–16], neurological diseases such as Parkinson's [17–19] and Alzheimers' [20–24] disease, and aging-related pathologies [25–28]. A common link between these pathologies is the presence of elevated levels of oxidative stress. Another disease state that is associated with increased levels of oxidative stress is that of metabolic syndrome, which encompasses several pathologies, including increased body weight and adiposity, fatty liver, elevated triglycerides, and impaired glucose tolerance.

While it is generally postulated that oxidative stress leads to progression of disease, the molecular mechanisms that mediate this process are as yet largely unknown. Since oxidative stress can lead to damage of cellular components, including DNA, we hypothesized that the absence of a critical DNA repair protein, such as in the case of OGG1-deficient mice, would lower the cellular tolerance for oxidative stress, such as that induced by consumption of a high-fat diet. We have therefore investigated the role of OGG1 in the development of metabolic disease and report here a novel role for OGG1 in the maintenance of cellular and whole body energy balance.

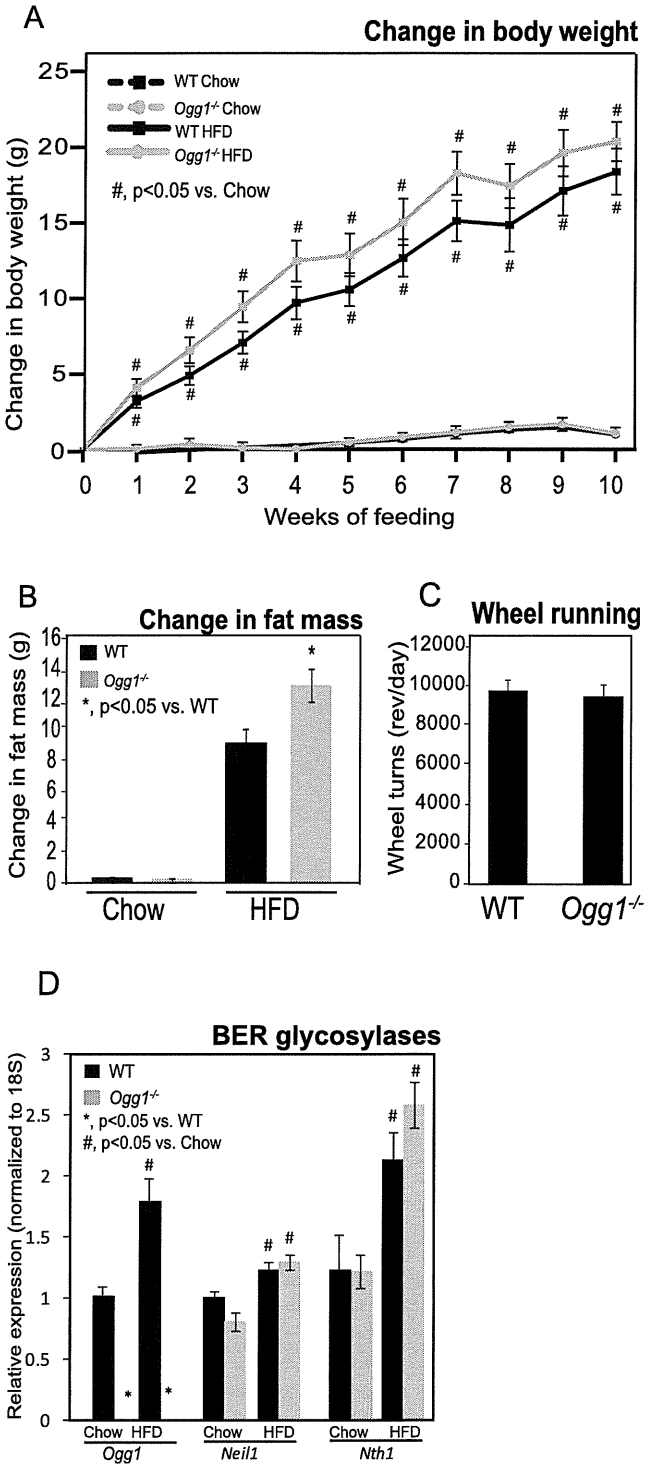

Figure 1. Body weight, body composition, voluntary activity, and gene expression of BER glycosylases. Body weights were measured weekly during the feeding period, and change in body weight from initial body weight was calculated (A). Body composition was measured by NMR at 0 and 4 weeks after the start of feeding, and change in fat mass was calculated (B). Voluntary physical activity was measured by recording wheel running in individually caged, chow-fed mice for 2 weeks (C). Expression of key glycosylases initiating BER of oxidized DNA was measured by qRT-PCR (D). *n = 6 for each group; *, p<0.05 vs. WT, #, p<0.05 vs. chow-fed mice.*
doi:10.1371/journal.pone.0051697.g001

Experimental Procedures

Animal Studies

The generation of *Ogg1*$^{-/-}$ mice backcrossed 21 times to C57BL/6J background has been previously described [15]. At OHSU, the *Ogg1*$^{-/-}$ allele was maintained through additional backcrossing to C57BL/6J and subsequent matings between *Ogg1*$^{+/-}$ mice. Age-matched male mice were exclusively used throughout this investigation. Six mice of each genotype were assigned to either chow diet or high-fat diet (HFD); this number was deemed to be the minimum required for adequate statistical power for the desired analyses based on our previous studies and similar reports in the literature. The breeding and care of animals are in accordance with the protocols approved by the Animal Care and Use Committee of Oregon Health & Science University, Portland, Oregon (Protocol Number A967). Prior to euthanasia by cervical dislocation, mice were anesthetized by CO_2 inhalation. For *in vivo* procedures, all efforts were made to minimize discomfort and suffering, in accordance with approved animal care protocols.?For the diet studies, 12-week old mice were individually housed and given *ad libitum* access to either rodent chow or a HFD (Research Diets D12492, New Brunswick, NJ; 60% fat, 20% protein, 20% carbohydrate by calories; 5.24 kcal/g metabolizable energy) for 10 weeks. Food intake and body weights were measured weekly during this period. Body composition was measured by low-resolution NMR (Echo Medical Systems, Houston, TX) prior to and 4 weeks after the start of the feeding study.

Energy Expenditure

Energy expenditure was measured by indirect calorimetry (Oxymax, Columbus Instruments, Columbus, OH) as previously described [29], after 4 weeks of feeding. Briefly, oxygen consumption (VO_2) and carbon dioxide production (VCO_2) were simultaneously determined in individually housed animals with *ad libitum* access to chow or HFD and water. Following a 48-hour acclimation period, VO_2 and VCO_2 were recorded for 24 hours, including a 12-hour dark and 12-hour light phase. Samples were recorded every 2 minutes with a room air reference taken every 12 minutes. Respiratory exchange ratio (RER) was calculated as the molar ratio of VCO_2: VO_2.

Glucose, Insulin, and Glycogen Measurements

Glucose tolerance was assessed 7 weeks after the start of the study and was carried out as previously described [29]. Briefly, mice were fasted for 4 hours followed by i.p. injection of 10% dextrose at a rate of 1g/kg body weight. Blood was collected at the indicated intervals for assessment of plasma glucose using the glucose color reagent (Cliniqa, San Marcos, CA). Fasting plasma insulin was measured by ELISA (Millipore, St. Charles, MO). Hepatic glycogen was measured by an enzyme coupled spectrophotometric assay, as previously described [29].

Tissue Collection and Pathology

At the end of 10 weeks of feeding, mice were euthanized by CO_2 overdose, and tissues were collected and snap frozen in liquid nitrogen for further analyses. For histological studies, liver and adipose tissues were fixed in buffered formalin and embedded in paraffin for sectioning and H&E staining. For transmission electron microscopy analyses, fresh liver sections were fixed and submitted to the Electron Microscopy Core at OHSU for sectioning and visualization. Buffer details are presented in Supplemental Methods.

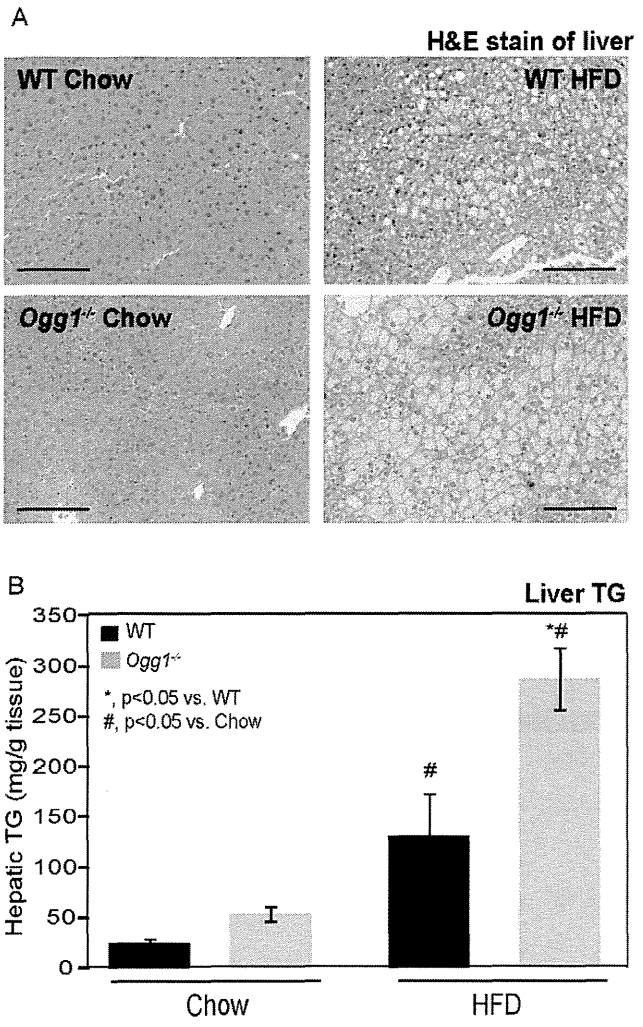

Figure 2. Hepatic lipid accumulation and triglyceride content. Hepatic lipids were visualized by H&E staining of formalin-fixed paraffin embedded liver tissues in chow- and HFD-fed animals (A). Images are representative of 3 animals per group. Bar represents 50 μM in all images. Hepatic triglyceride (TG) content (B) was quantified as described. *n = 6 for each group; *, p<0.05 vs. WT, #, p<0.05 vs. chow-fed mice.*

doi:10.1371/journal.pone.0051697.g002

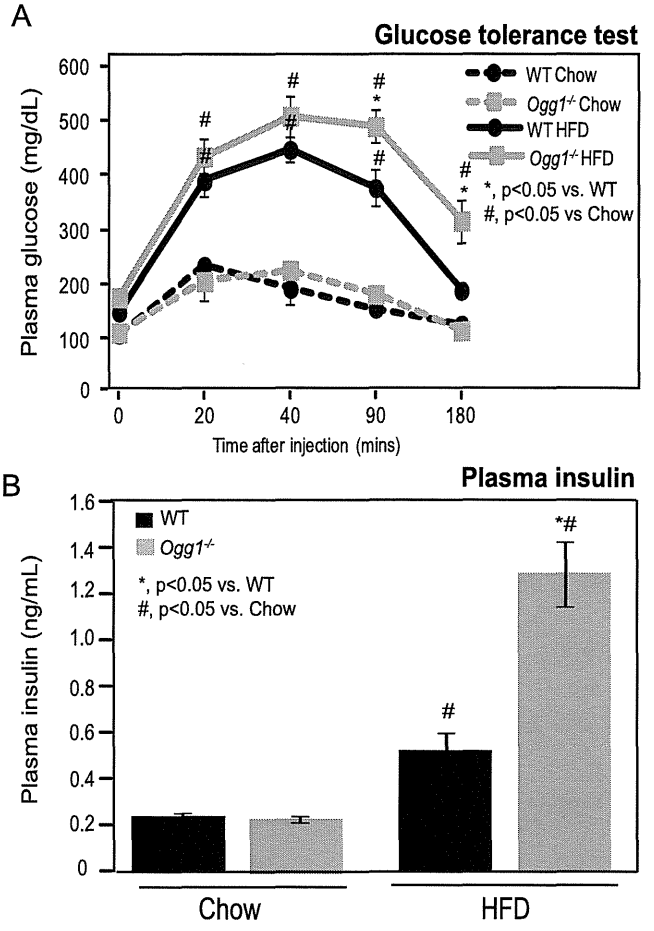

Figure 3. Glucose tolerance and plasma insulin. Glucose tolerance was measured by quantifying plasma glucose after an intraperitoneal injection of 1g glucose/kg BW in chow-fed and HFD-fed animals (A). Fasting plasma insulin was measured by ELISA prior to glucose injection (B). *n = 6 for each group; *, p<0.05 vs. WT, #, p<0.05 vs. chow-fed mice.*

doi:10.1371/journal.pone.0051697.g003

Tissue and Plasma Lipids

Total hepatic triglycerides (TG) were analyzed using the Wako total TG kit (Wako Chemicals, Richmond, VA). For fasting plasma ketone analyses, age-matched mice were fasted overnight, and blood was collected via saphenous vein puncture. Plasma ketones were measured using the plasma β-hydroxybutyrate kit (Cayman Chemical Co., Ann Arbor, MI).

Physical Activity

Voluntary physical activity was assessed in chow-fed 12-week old male mice, as previously described [30]. Briefly, mice were acclimated to individual housing in shoebox cages equipped with running wheels for 7 days, and voluntary wheel running was measured for 2 consecutive weeks. Activity was monitored automatically using a Mini Mitter Magnetic Switch and the VitalView Data Acquisition System (Mini Mitter, Sun River, OR).

Mitochondrial DNA Quantitation and Gene Expression Analysis

Mitochondrial DNA content was measured as previously described [29]. DNA microarray experiments were conducted at the Affymetrix Microarray Core of the OHSU Gene Microarray Shared Resource. Gene expression was measured using the Mouse Gene ST GeneChip Array (Affymetrix, Inc., Santa Clara, Calif, www.affymetrix.com). Data visualization and exploratory analysis were conducted using GeneSifter web-based software, release 59.0 (GeoSpiza Inc., Seattle, WA). Analysis, quality control, and statistical methods are presented in Supplemental Methods. All microarray data has been deposited in GEO and may be accessed via accession number GSE35497. RNA for quantitative real-time PCR (qPCR) was isolated using Tri-reagent RT (MRC, Inc., Cincinnati, OH). 1 μg of RNA was reverse-transcribed using the Superscript III first-strand synthesis system (Invitrogen, Carlsbad, CA). qPCR was performed on a Bio-Rad iCycler qPCR instrument (Bio-Rad, Hercules, CA) using gene-specific primers. Gene expression was normalized to expression of 18S rRNA. Primer sequences are available upon request.

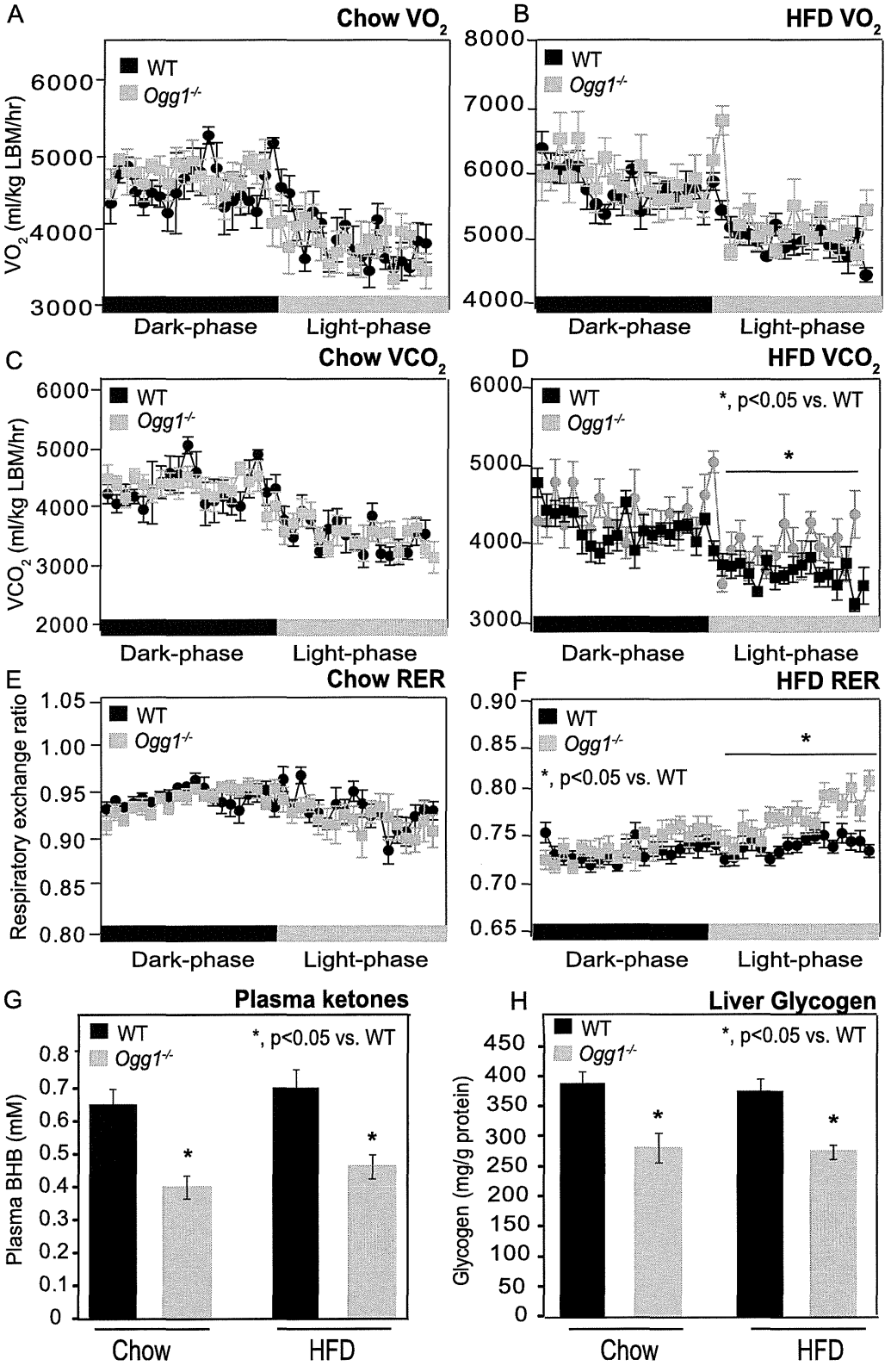

Figure 4. Indirect calorimetry, plasma ketones, and hepatic glycogen. O_2 consumption (A, B), and CO_2 production (C, D) were measured by indirect calorimetry in chow- or HFD-fed animals over consecutive dark and light cycles. Respiratory exchange ratio (RER) was calculated as VCO_2/VO_2 (E, F). Fasting plasma ketones were measured after an overnight fast (G). Hepatic glycogen (H) was measured in chow-fed and HFD-fed *Ogg1*$^{-/-}$ mice. *n = 6 in each group; *, p<0.05 vs. WT.*
doi:10.1371/journal.pone.0051697.g004

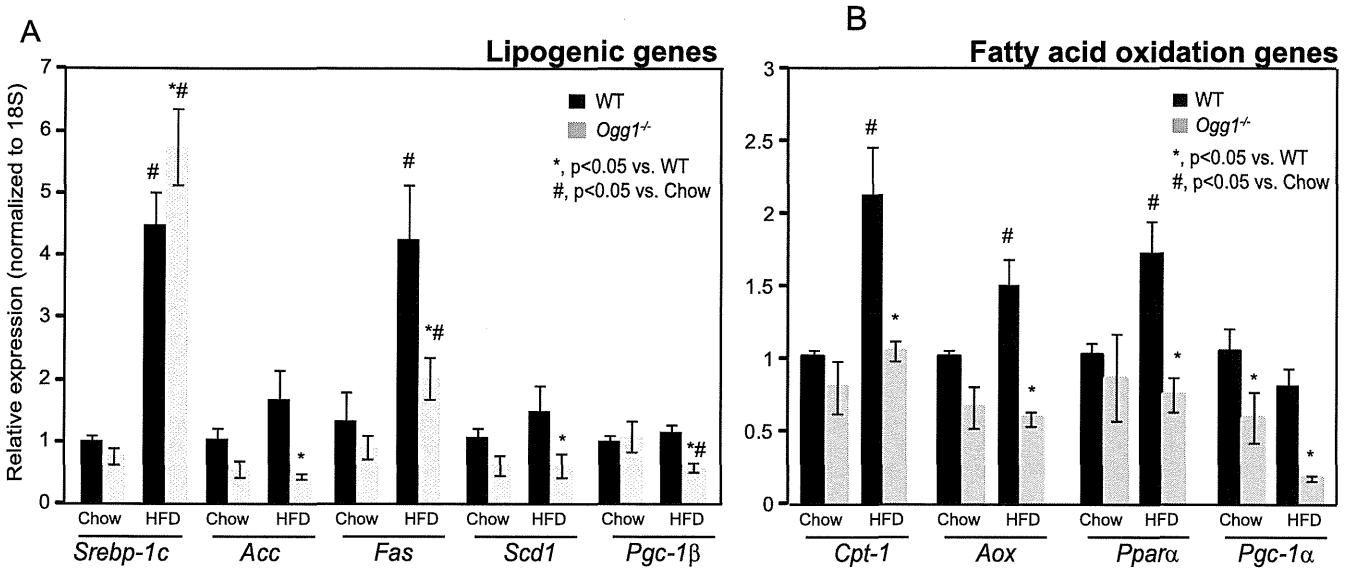

Figure 5. Hepatic lipogenic and fatty acid oxidation gene expression. Expression of key genes involved in hepatic lipogenesis (A) and fatty acid oxidation (B) were measured by qRT-PCR. n = 6 in each group; *, *p<0.05 vs. WT*, #, *p<0.05 vs. chow-fed mice.*
doi:10.1371/journal.pone.0051697.g005

Statistical Analyses

Data are expressed as mean±SEM with comparisons carried out using student's t-test for two-group comparisons (Figure 1C) or one-way ANOVA followed by post-hoc analysis using a multiple comparison procedure with Bonferroni/Dunn post-hoc comparison in Graphpad Prism. p-values <0.05 were considered significant.

Results

Ogg1$^{-/-}$ mice have an Increased Propensity to Adiposity, Especially Upon High-fat Diet Feeding

In a previous study examining potassium bromate-induced carcinogenesis in *Ogg1*$^{-/-}$ mice, data were also presented that suggested a trend towards increased body weights in *Ogg1*$^{-/-}$ mice, relative to wild-type (WT) counterparts that were maintained on a chow diet [31]. In order to determine if body weights and body composition are indeed significantly altered in *Ogg1*$^{-/-}$ animals, male mice were individually housed at 12 weeks of age and given *ad libitum* access to either chow or a hypercaloric high-fat diet (HFD). Over the duration of the 10-week study, chow-fed WT and *Ogg1*$^{-/-}$ mice displayed similar body weights (Figure 1A). HFD-feeding significantly increased weight gain in all mice, with WT mice gaining 17.5 g on average and *Ogg1*$^{-/-}$ counterparts gaining 20.4 g over 10 weeks of feeding (Figure 1A). However, total weight gain over the 10-week feeding period was not significantly different between WT and *Ogg1*$^{-/-}$ mice on either chow or HFD (Figure 1A). Although chow-fed *Ogg1*$^{-/-}$ mice were not significantly heavier at the end of the feeding study, in a separate cohort of animals allowed to age to 12–15 months on a chow diet, *Ogg1*$^{-/-}$ mice weighed 45.1±1.40 g (n = 5) on average, compared to WT counterparts that weighed 34.5±0.87 g (n = 6; p<0.05).

In addition to body weight, body composition was also measured by NMR before and 4 weeks after the start of feeding. Fat accumulation was significantly higher in HFD-fed *Ogg1*$^{-/-}$ mice, compared to WT counterparts (Figure 1B). While WT mice gained 9.14 g of fat (a 23% increase) upon HFD-feeding, *Ogg1*$^{-/-}$

Table 1. Fatty acid oxidation genes.

Gene ID	Fold change	Direction	adjusted p-value	Fold change qRT-PCR	Direction	p-value
Cab39l	2.08	Down	0.00327	3.72	Down	7.73E-05
Etfdh	2.05	Down	0.002688	3.43	Down	0.000125
Acsl5	1.93	Down	0.011995	3.12	Down	0.00311
Prkaa2	1.88	Down	0.004445	2.98	Down	0.001322
Ppargc1a	1.73	Down	0.00455	4.78	Down	0.00406207
Acadm	1.51	Down	0.007172	2.26	Down	0.001677
Peci	1.51	Down	0.009513	1.91	Down	0.038155

Genes associated with fatty acid oxidation were identified from among the significantly differentially expressed probe sets between HFD-fed WT and *Ogg1*$^{-/-}$ mice, using gene ontology terms in Gene Sifter. Gene expression changes were confirmed by qRT-PCR using gene-specific primers. n = 6 in each group. *Cab39l*, calcium binding protein 39-like, *Etfdh*, electron transfer flavoprotein-ubiquinone oxidoreductase, *Acsl5*, acyl-CoA synthetase 5, *Prkaa2*, 5′-AMP-activated protein kinase catalytic subunit alpha-2, *Ppargc1a*, Peroxisome proliferator-activated receptor gamma coactivator 1-alpha, *Acadm*, medium-chain acyl-CoA dehydrogenase, *Peci*, peroxisomal 3,2-trans-enoyl-CoA isomerase.
doi:10.1371/journal.pone.0051697.t001

Table 2. TCA cycle metabolism genes.

Gene ID	Fold change	Direction	adjusted p-value	Fold change qRT-PCR	Direction	p-value
Dld	1.68	Down	0.013095	2.95	Down	0.000386
Mdh1	1.64	Down	0.004434	3.29	Down	0.000167
Fh1	1.63	Down	0.006485	3.06	Down	0.001282
Idh3a	1.48	Down	0.003829	2.02	Down	0.001583
Pdha1	**1.35**	Down	0.00929	1.86	Down	0.003487
Sucla2	**1.32**	Down	0.016633	2.10	Down	0.006097
Aco1	**1.28**	Down	0.003759	1.34	Down	0.013955
Sdha	**1.20**	Down	0.010029	1.56	Down	0.015946

Genes associated with TCA cycle metabolism were identified from among the significantly differentially expressed probe sets between HFD-fed WT and *Ogg1*$^{-/-}$ mice, using gene ontology terms in Gene Sifter. Gene expression changes were confirmed by qRT-PCR using gene-specific primers. $n=6$ in each group. *Idh3a*, isocitrate dehydrogenase 3, *Pdha1*, pyruvate dehydrogenase E1 alpha 1, *Sucla2*, succinate-Coenzyme A ligase, *Aco1*, aconitase 1, *Sdha*, succinate dehydrogenase complex, subunit A.

doi:10.1371/journal.pone.0051697.t002

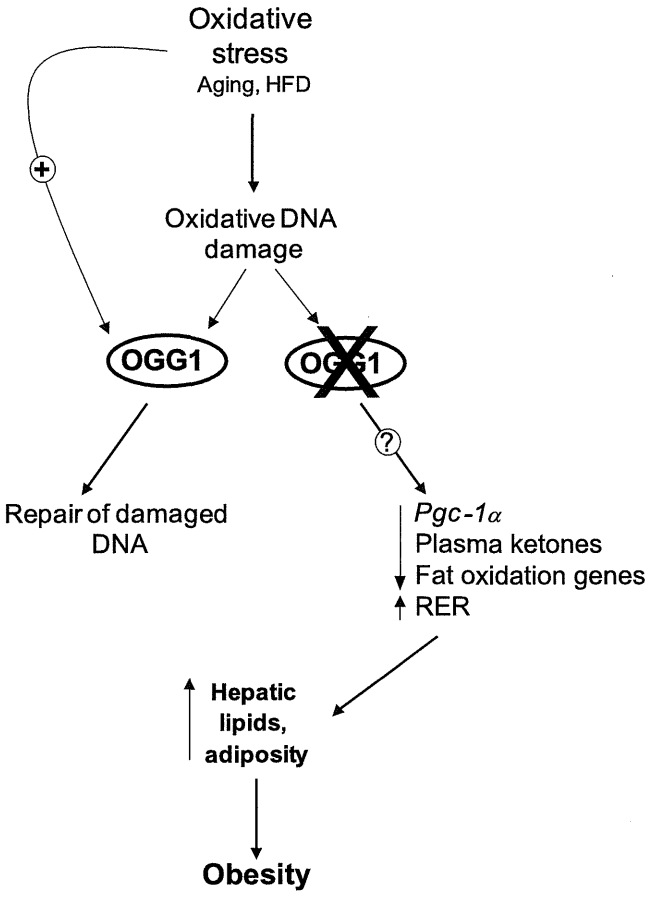

Figure 6. Proposed model for maintenance of metabolic health by OGG1. Oxidative stress, such as that induced by consumption of a HFD, damages cellular components, including DNA. Key BER glycosylases, such as *Ogg1*, are induced in response to this stress and help to restore genomic integrity. In contrast, in the absence of OGG1, through mechanisms that are as yet unclear, there is aberrant regulation of downstream factors such as *Pgc-1α* and fatty acid oxidation. These alterations lead to a potential fat-sparing phenotype in OGG1-deficient mice, resulting in accelerated development of hepatic steatosis and obesity upon HFD-feeding in *Ogg1*$^{-/-}$ mice.

doi:10.1371/journal.pone.0051697.g006

mice gained 12.95 g of fat (a 28% increase) in the same period (Figure 1B). By 12–15 months of age, body fat in the aged cohort maintained on chow diet was also significantly different, with aged *Ogg1*$^{-/-}$ animals having 32.2% of their body weight as fat mass, compared to 19.5% body fat in WT counterparts ($p<0.05$). These data indicate that *Ogg1*$^{-/-}$ mice have an increased propensity to adiposity with age or in response to HFD-feeding, compared to WT controls.

At the end of the feeding period, visceral and subcutaneous adipose depots were collected and weighed. Both visceral (2.66 ± 0.12 in WT vs. 2.91 ± 0.19 g in *Ogg1*$^{-/-}$; $p>0.05$) and subcutaneous (0.92 ± 0.09 in WT vs. 1.28 ± 0.06 g in *Ogg1*$^{-/-}$; $p<0.05$) adipose depots tended to be larger in HFD-fed *Ogg1*$^{-/-}$ mice, relative to WT counterparts, indicating a generalized increase in fat accumulation in these mice. Voluntary activity (Figure 1C) and food intake were not significantly different between WT and *Ogg1*$^{-/-}$ mice either on chow (4.14 ± 0.19 g in WT vs. 4.10 ± 0.18 g in *Ogg1*$^{-/-}$) or HFD (2.91 ± 0.15 g in WT vs. 3.21 ± 0.19 g in *Ogg1*$^{-/-}$).

While a HFD is known to induce oxidative stress, the effect of extended high-fat feeding on expression of BER glycosylases has not been characterized. Therefore, we measured the expression of three key BER glycosylases, *Ogg1*, *Neil1*, and *Nth1*, in livers of chow- and HFD-fed mice (Figure 1D). HFD-feeding increased expression of all three glycosylases in WT mice, suggesting that the BER pathway is upregulated in response to HFD-feeding. *Neil1* and *Nth1* expression were increased by HFD-feeding in *Ogg1*$^{-/-}$ mice, as well. As expected, *Ogg1* expression was undetectable in *Ogg1*$^{-/-}$ animals.

Ogg1$^{-/-}$ mice have Increased Hepatic Lipid Accumulation and Impaired Glucose Tolerance

Hepatic lipid accumulation was visualized by H&E staining, and total hepatic TG was quantified. Under chow-fed conditions, there were no significant differences in hepatic TG levels between WT and *Ogg1*$^{-/-}$ mice (Figures 2A, B). However, HFD-fed *Ogg1*$^{-/-}$ mice had a more than 2-fold higher accumulation of hepatic TG, compared to WT animals (Figures 2A, B).

Since increased adiposity and hepatic lipid accumulation are risk factors for insulin resistance, glucose tolerance was assessed after 7 weeks of chow or HFD-feeding. After an intraperitoneal injection of glucose, chow-fed mice showed an increase in plasma glucose that returned to baseline levels by 180 minutes after injection (Figure 3A). As anticipated, HFD-feeding resulted in

greater elevations in plasma glucose after glucose injection. While starting plasma glucose levels were comparable to WT values in HFD-fed *Ogg1*$^{-/-}$ mice, glucose clearance was significantly delayed in these animals. Plasma glucose levels at 90 and 180 minutes after glucose injection were significantly higher in HFD-fed *Ogg1*$^{-/-}$ mice, relative to WT counterparts (Figure 3A). Fasting plasma insulin levels were comparable in chow-fed WT and *Ogg1*$^{-/-}$ mice (Figure 3B). HFD-feeding increased fasting plasma insulin levels by 2.2-fold in WT mice and by 5.8-fold in *Ogg1*$^{-/-}$ animals (Figure 3B). In conjunction with the delayed glucose clearance (Figure 3A), the elevated plasma insulin levels in HFD-fed *Ogg1*$^{-/-}$ mice (Figure 3B) indicate a significant impairment in insulin sensitivity in these animals, relative to WT controls.

Resting Respiratory Exchange Ratio, Fasting Plasma Ketones, and Hepatic Glycogen Content are Altered in *Ogg1*$^{-/-}$ mice

In order to determine if basal metabolic rates were altered due to OGG1 deficiency, O_2 consumption and CO_2 production were measured in chow and HFD-fed mice. There were no significant differences in O_2 consumption or CO_2 production between chow-fed WT and *Ogg1*$^{-/-}$ mice (Figures 4A and 4B). After HFD-feeding, CO_2 production during the resting phase was significantly higher in *Ogg1*$^{-/-}$ mice, relative to WT animals (Figure 4C and 4D). Consistently, the respiratory exchange ratio (RER), an indicator of substrate utilization, was also significantly increased during the resting phase in HFD-fed *Ogg1*$^{-/-}$ mice (Figure 4F), relative to WT animals, indicating a slight, but significant decrease in reliance on fatty acid oxidation for energy needs during the resting phase in these animals.

Fasting plasma ketones were measured after an overnight fast to obtain an additional measure of *in vivo* fatty acid oxidation. Interestingly, in chow-fed *Ogg1*$^{-/-}$ mice, fasting plasma ketones were reduced by 39% ($p<0.05$), relative to WT controls (Figure 4G). HFD-fed *Ogg1*$^{-/-}$ mice also had a similar 34% decrease ($p<0.05$) in fasting plasma ketones, indicating reduced rates of fatty acid oxidation in *Ogg1*$^{-/-}$ mice.

Based on the significant increase in RER (Figure 4F), we hypothesized that *Ogg1*$^{-/-}$ mice may preferentially utilize carbohydrate stores to meet energy needs. Therefore, hepatic glycogen content was measured and found to be diminished by 27% ($p<0.05$) in both chow-fed and HFD-fed *Ogg1*$^{-/-}$ mice, relative to WT counterparts (Figure 4H). Concomitantly, we also observed a slight, but significant increase in gene expression of two rate-limiting glycolytic enzymes, glucokinase (32%; $p<0.05$) and phosphofructokinase (23%; $p<0.05$), in livers of HFD-fed *Ogg1*$^{-/-}$ mice. Taken together with the reduced fasting plasma ketones and the significant increase in resting phase RER, these data are suggestive of a decreased reliance on fatty acids as a fuel source in *Ogg1*$^{-/-}$ mice.

Since OGG1 has both nuclear and mitochondrial localization, we sought to determine if mtDNA content or mitochondrial structure was altered in *Ogg1*$^{-/-}$ mice. mtDNA abundance was measured by PCR and was not consistently reduced in all *Ogg1*$^{-/-}$ mice (Supporting Figure S1A). TEM analysis of mitochondrial density and ultrastructure in liver did not reveal differences between WT and *Ogg1*$^{-/-}$ mice (Supporting Figure S1B).

Hepatic Lipogenic Genes are not Upregulated in *Ogg1*$^{-/-}$ Livers

To gain further insight into the mechanistic changes underlying the metabolic phenotype of *Ogg1*$^{-/-}$ animals, hepatic gene expression was assessed through a combination of high-throughput DNA microarray and quantitative real-time PCR (qPCR). Analysis of differentially expressed probe sets (DEPs) by GeneSifter revealed 26 probesets (10 upregulated, 16 downregulated) to be altered by at least 1.5 fold in chow-fed *Ogg1*$^{-/-}$ livers, compared to WT livers (Supporting Table S1). After 10 weeks of HFD feeding, 1572 probesets were differentially expressed (132 upregulated and 1440 downregulated) in *Ogg1*$^{-/-}$ livers, compared to WT counterparts (Supporting Table S2). In addition to data analysis by GeneSifter, the Affymetrix data was simultaneously submitted to Ingenuity Systems for analysis via Ingenuity iReport for Gene Expression Analysis, the results of which were over 75% concordant with the GeneSifter analyses (Supporting Tables S3, S4). To investigate possible biological interactions and commonalities between the differentially regulated genes, DEPs identified by GeneSifter analyses were analyzed using Kyoto Encyclopedia of Genes and Genomes (KEGG) and gene ontology terms in GeneSifter, and pathways with a z-score greater than or equal to 2.0 and less than or equal to −2.0 were considered to be enriched or underrepresented, respectively (Supporting Tables S5, S6).

Given the observations of metabolic dysfunction in *Ogg1*$^{-/-}$ mice, the microarray data were queried for potential mechanisms that may explain these phenotypes. Since increased hepatic TG can occur secondary to increased *de novo* lipogenesis, we sought to determine if hepatic lipogenic genes were differentially regulated in livers of *Ogg1*$^{-/-}$ mice. The master regulator of lipogenic genes, sterol regulatory element binding protein-1c (SREBP-1c, gene ID: *Srebf*), which also regulates its own gene expression, was increased by 1.9-fold in livers of HFD-fed *Ogg1*$^{-/-}$ mice (Supporting Tables S2, S4). Interestingly, none of the classical target genes of SREBP-1c, including acetyl-CoA carboxylase (*Acc*), fatty acid synthase (*Fas*) or stearoyl-CoA desaturase-1 (*Scd1*) were found to be upregulated by either microarray or by qPCR analyses (Figure 5A). In fact, all these genes were significantly lower in livers of HFD-fed *Ogg1*$^{-/-}$ mice, relative to WT counterparts. The expression of PPAR gamma co-activator -1β (*Pgc-1β*), a requisite co-activator of SREBP-1c, was also significantly lower in HFD-fed *Ogg1*$^{-/-}$ mice, relative to WT mice (Figure 5A). This downregulation of *Pgc1-β* may explain the lack of increase in hepatic lipogenic gene expression, despite a significant induction of *Srebp-1c*. Nevertheless, based on these results, the increase in hepatic lipids in *Ogg1*$^{-/-}$ mice (Figure 2A) does not appear to be a consequence of increased hepatic lipogenesis.

Fatty Acid Oxidation and TCA Cycle Gene Expression is Reduced in *Ogg1*$^{-/-}$ Livers

Since resting phase RER was significantly higher and plasma ketones were reduced in HFD-fed *Ogg1*$^{-/-}$ mice, expression of genes involved in fat oxidation was examined. Consistent with a reduction in fatty acid oxidation, the microarray data revealed that several genes involved in fatty acid oxidation were significantly downregulated in HFD-fed *Ogg1*$^{-/-}$ livers, relative to WT counterparts (Table 1). Calcium-binding protein 39-like (*Cab39l*; also termed mouse protein 25 beta), electron-transferring-flavoprotein dehydrogenase (Etfdh), long-chain acyl-coenzymeA (CoA) synthetase isoforms 5 (*Acsl5*), AMP-activated protein kinase alpha subunit 2 (AMPKα2), PPAR-gamma coactivator -1 alpha (*Pgc-1α*), medium chain acyl-Coenzyme A dehydrogenase (*Acadm*), and peroxisomal enoyl-CoA delta isomerase (*Peci*), were all significantly downregulated by at least 1.5-fold in HFD-fed *Ogg1*$^{-/-}$ livers (Table 1). Furthermore, *Pgc-1α*, a key regulator of fatty acid oxidation gene expression in liver, was significantly lower in livers of chow-fed (Figure 5B), as well as HFD-fed (Table 1 and

Figure 5B) *Ogg1*$^{-/-}$ mice. Concomitant with the reduction in *Pgc-1α*, additional key genes of fatty acid oxidation, including carnitine palmitoyl transferase-1 (*Cpt-1*), acyl CoA oxidase (*Aox*), and peroxisome proliferator-activated receptor alpha (*Pparα*)? were also decreased in HFD-fed *Ogg1*$^{-/-}$ mice, relative to WT counterparts (Figure 5B).

In addition to fatty acid oxidation, PGC-1α also regulates genes involved in TCA cycle metabolism [32]. Consistent with the reduction in *Pgc-1α* levels (Table 1 and Figure 5B), several genes involved in the TCA cycle, including dihydrolipoamide dehydrogenase (*Dld*), malate dehydrogenase 1 (*Mdh1*), and fumarate hydratase (Fh) were all reduced by at least 1.5 fold in HFD-fed *Ogg1*$^{-/-}$ mice, as indicated by microarray analysis (Table 2). Additional genes involved in TCA cycle metabolism including isocitrate dehydrogenase 3 (*Idh3a*), pyruvate dehydrogenase E1 alpha 1 (*Pdha1*), succinate-Coenzyme A ligase (*Sucla2*), aconitase 1 (*Aco1*), succinate dehydrogenase complex, subunit A (*Sdha*) were all downregulated by at least 20% in HFD-fed *Ogg1*$^{-/-}$ livers (Table 2).

Discussion

We demonstrate here that the DNA repair glycosylase, OGG1, plays a novel role in regulating cellular energy metabolism. *Ogg1* expression is induced in response to a HFD (Figure 1D), suggesting that the repair of oxidative lesions such as 8-oxo-G by OGG1 are part of the cellular response to oxidative stress, such as that induced by a HFD. Conversely, in the absence of OGG1, a HFD led to accelerated development of several features of metabolic syndrome, including increased adiposity (Figure 1B), hepatic lipid accumulation (Figure 2), and impaired glucose tolerance upon high-fat feeding (Figure 3A). This was accompanied by increased resting RER (Figure 4F), reduced fasting plasma ketones (Figure 4G), and reduced expression of key genes of fat oxidation (Table 1 and Figure 5B), all indicating a shift in energy metabolism in *Ogg1*$^{-/-}$ mice away from fat oxidation. Taken together with the reduced hepatic glycogen content in *Ogg1*$^{-/-}$ livers (Figure 4H), these changes are indicative of a shift in cellular metabolism towards glucose utilization, over fat oxidation, in *Ogg1*$^{-/-}$ livers.

Regulation of *Pgc-1* Transcriptional Co-activators and Fatty Acid Oxidation in Response to DNA Damage

A striking observation in *Ogg1*$^{-/-}$ mice was that of reduced levels of both *Pgc-1α* and *-1β* expression in liver. These two highly regulated transcriptional co-activators play critical roles in diverse cellular processes [33–35]. PGC-1β is a requisite co-activator for the lipogenic transcription factor, SREBP-1c [36]. Therefore, the reduction in *Pgc-1β* levels (Figure 5A) in *Ogg1*$^{-/-}$ livers may explain the lack of induction of *de novo* lipogenesis in *Ogg1*$^{-/-}$ mice, despite a significant increase in *Srebp-1c* message levels (Figure 5A).

PGC-1α plays tissue-specific roles in pathways ranging from mitochondrial biogenesis [35] to TCA cycle flux [32] and fatty acid oxidation [33]. Chow-fed and HFD-fed *Ogg1*$^{-/-}$ mice had significantly reduced expression of hepatic *Pgc-1α*, compared to WT counterparts. Consistently, while expression of *Cpt-1*, a *Pgc-1α* target gene, was significantly elevated in response to HFD-feeding in WT mice (Figure 5B), *Ogg1*$^{-/-}$ animals did not show a similar induction of *Cpt-1*. Furthermore, several additional genes of fatty acid oxidation were found to be reduced, especially after HFD-feeding, in *Ogg1*$^{-/-}$ mice (Table 1 and Figure 5B). In addition to these changes in gene expression, *Ogg1*$^{-/-}$ mice also had significantly reduced plasma ketone levels following an overnight fast (Figure 4G), suggesting decreased fatty acid oxidation, consistent with the observation of elevated resting phase RER (Figure 4F) in these mice.

The observation of reduced levels of *Pgc-1α* in *Ogg1*$^{-/-}$ mice after HFD is especially striking. PGC-1α has been demonstrated to be downregulated in response to DNA damage via both reduced transcription of the gene [37], as well as through increased protein degradation [3]. Furthermore, several groups have reported a decrease in *Pgc-1α* levels in breast and colon cancers [38–40]. Given the role of OGG1 in maintaining genomic integrity, it is therefore plausible that the reduction of *Pgc-1α* upon HFD-feeding is directly or indirectly related to the DNA repair functionality of OGG1, and that this downregulation of *Pgc-1α* mediates the metabolic phenotype observed in *Ogg1*$^{-/-}$ mice. Additional studies are underway in order to understand the precise nature of the downregulation of *Pgc-1α* in *Ogg1*$^{-/-}$ mice, including regulation of the PGC-1α protein. However, from the current study, it is clear that OGG1 deficiency alters the hepatic response to a HFD such that expression of *Pgc-1α*, as well as that of several of its key downstream target genes, is blunted in *Ogg1*$^{-/-}$ mice. To our knowledge, this is the first demonstration of a DNA repair protein being directly linked to the dietary regulation of *Pgc-1α* and as such, provides important potentially mechanistic information regarding the pathology of diet-induced metabolic disease.

OGG1 Deficiency is Correlated with Human Metabolic Disease

In further support for a role for OGG1 in metabolic dysfunction, the Ser326Cys OGG1 polymorphism has been recently reported to be associated with Type II diabetes in both a Japanese and Mexican American population [41,42]. While most studies investigating the consequences of human OGG1 polymorphisms have thus far been focused on the role of OGG1 in carcinogenesis, in light of the emerging evidence suggesting a role for OGG1 in maintaining energy balance, it will be interesting to determine if these common polymorphisms of human OGG1 are also associated with features of the metabolic syndrome. To our knowledge, studies investigating common gene polymorphisms and their correlations with increased body mass index have not thus far focused extensively on a role for DNA repair glycosylases such as *Ogg1* or *Neil1*. Given the emerging link between these glycosylases and metabolic syndrome, a retrospective screen of specimens collected in previous studies may help shed light on potential correlations between inactivating mutations in *Ogg1* and metabolic disease. In this regard, ongoing studies in our lab are aimed at characterizing the prevalence of common polymorphisms in the *Ogg1* gene, as well as the extent of tissue DNA damage in cohorts such as individuals undergoing bariatric surgery to determine the incidence of inactivating mutations in DNA repair genes in obese populations.

OGG1 Acts through a Distinct Mechanism in Regulating Metabolic Parameters

We previously described a phenotype of spontaneous obesity and metabolic dysfunction in mice deficient in another BER glycosylase, NEIL1 [29,43]. *Neil1*$^{-/-}$ mice spontaneously develop obesity on a chow diet, a phenotype that is greatly accelerated by HFD-feeding [29,43]. This is accompanied by increased hepatic lipid accumulation and impairments in glucose tolerance in *Neil1*$^{-/-}$ mice [29,43]. Since NEIL1 and OGG1 have very distinct substrate specificities in the repair of oxidized lesions, these similarities in phenotype with regard to the development of metabolic syndrome were completely unexpected. Indeed, a similar phenotype has not been observed in mice deficient in NEIL3 [44],

despite considerable overlap in substrate specificities between NEIL1 and NEIL3. Interestingly, despite broad similarities in phenotype between *Neil1*$^{-/-}$ and *Ogg1*$^{-/-}$ mice, these two models exhibit important differences in the mechanisms underlying the observed pathologies. While overall energy expenditure was reduced in *Neil1*$^{-/-}$ mice [29], we did not observe any specific changes in RER [29] or fasting ketones in *Neil1*$^{-/-}$ animals (Sampath, Lloyd; unpublished), suggesting a generalized decrease in metabolic rate in *Neil1*$^{-/-}$ mice, rather than altered substrate preference, as observed in *Ogg1*$^{-/-}$ animals (Figures 4D,F). Furthermore, gene expression analysis of livers of *Neil1*$^{-/-}$ mice revealed a marked increase in inflammatory gene expression [29], while such a phenotype was not evident in the *Ogg1*$^{-/-}$ mice in the current study. This lack of an inflammatory response in *Ogg1*$^{-/-}$ livers, despite increased lipid accumulation, is consistent with other reports of an attenuated inflammatory response in the absence of OGG1 [45,46], suggesting a possible role for excision of 8-oxoG and its subsequent release into the circulation in modulating the tissue inflammatory response.

Based on the results of the current study, we propose that oxidative stress, such as that resulting from HFD-feeding, results in DNA damage and a compensatory upregulation of the BER pathway to address this damage (Figures 1D, 6). In the absence of OGG1, a critical enzyme of the BER system, DNA damage goes unrepaired, leading to an aberrant response to a HFD in terms of regulation of *Pgc-1α* expression and fatty acid oxidation (Figures 4D, 4F, 4G, 5B, 6). Misregulation of these mediators leads to sparing of fat as a fuel and ultimately to lipid accumulation and obesity in *Ogg1*$^{-/-}$ mice (Figures 1B, 2, 6). These findings shed light on a novel pathway of metabolic regulation downstream of DNA damage and argue for an unexpected but critical role for OGG1 and the BER pathway in the maintenance of whole body energy balance.

Supporting Information

Figure S1 Mitochondrial DNA content and mitochondrial ultrastructure. Mitochondrial DNA content (A, B) was measured by PCR using primers directed against two different regions of mitochondrial DNA. n = 5–6 in each group. CytoxII, cytochrome c oxidase, subunit 2; ND5, NADH dehydrogenase subunit 5. Mitochondrial density and ultrastructure in liver was also visualized by TEM (C). Images are representative of 3 animals per group. Scale bar represents 8.33 μM in all images.
(TIF)

Table S1 Differentially expressed probesets (DEPs) identified by GeneSifter in chow-fed *Ogg1*$^{-/-}$ livers. Pairwise analysis of chow-fed WT vs. *Ogg1*$^{-/-}$ was performed by t-test between the groups, followed by a Benjamini and Hochberg adjustment used to correct for false discovery rates using GeneSifter software. WT mice were designated as the control group, and *Ogg1*$^{-/-}$ mice were designated as the experimental group. Probesets that were differentially expressed by at least 1.5 fold and with an adjusted $p<0.05$ are presented. n = 6 in each group.
(DOC)

Table S2 DEPs identified by GeneSifter in HFD-fed *Ogg1*$^{-/-}$ livers. Pairwise analysis of HFD-fed WT vs. *Ogg1*$^{-/-}$ was performed by t-test between the groups, followed by a Benjamini and Hochberg adjustment used to correct for false discovery rates using GeneSifter software. WT mice were designated as the control group, and *Ogg1*$^{-/-}$ mice were designated as the experimental group. Probesets that were differentially expressed by at least 1.5 fold and with an adjusted $p<0.05$ are presented. n = 6 in each group.
(DOC)

Table S3 DEPs identified by iReport in chow-fed *Ogg1*$^{-/-}$ livers. Pairwise analysis of chow-fed WT vs. *Ogg1*$^{-/-}$ was conducted by iReport (Ingenuity Systems, Redwood City, CA), with WT mice were designated as the control group, and *Ogg1*$^{-/-}$ mice designated as the experimental group. Probesets that were differentially expressed by at least 1.5 fold and with an adjusted $p<0.05$ are presented. n = 6 in each group.
(DOC)

Table S4 DEPs identified by iReport in HFD-fed *Ogg1*$^{-/-}$ livers. Pairwise analysis of HFD-fed WT vs. *Ogg1*$^{-/-}$ was conducted by iReport (Ingenuity Systems, Redwood City, CA), with WT mice were designated as the control group, and *Ogg1*$^{-/-}$ mice designated as the experimental group. Probesets that were differentially expressed by at least 1.5 fold and with an adjusted $p<0.05$ are presented. n = 6 in each group.
(DOC)

Table S5 KEGG Pathway analysis of DEPs in chow-fed *Ogg1*$^{-/-}$ livers. DEPs that were altered by at least 1.4 fold in chow-fed *Ogg1*$^{-/-}$ livers, relative to WT livers, were annotated using the Kyoto Encyclopedia of Genes and Genomes (KEGG) in GeneSifter. All pathways with an associated z-score >2.0 or <-2.0 are presented. n = 6 per group. n = 6 in each group.
(DOC)

Table S6 KEGG Pathway analysis of DEPs in HFD-fed *Ogg1*$^{-/-}$ livers. DEPs that were altered by at least 1.4 fold in HFD-fed *Ogg1*$^{-/-}$ livers, relative to WT livers, were annotated using the Kyoto Encyclopedia of Genes and Genomes (KEGG) in GeneSifter. All pathways with an associated z-score >2.0 or <-2.0 are presented. n = 6 per group.
(DOC)

Methods S1 Supporting Methods.
(DOC)

Acknowledgments

We would like to thank Drs. Daniel Marks and Lisa Wood (OHSU, Portland, OR) for the use of small animal MRI and indirect calorimetry chambers, and wheel running cages, respectively; Dr. Peter Spencer (OHSU) for interpretation of TEM images; and Drs. James Ntambi (UW-Madison) and Amanda McCullough (OHSU) for valuable discussions.

Author Contributions

Conceived and designed the experiments: HS RSL. Performed the experiments: HS VV MRR. Analyzed the data: HS RSL. Contributed reagents/materials/analysis tools: KS YN. Wrote the paper: HS YN RSL.

References

1. Nemec AA, Wallace SS, Sweasy JB (2010) Variant base excision repair proteins: contributors to genomic instability. Semin Cancer Biol 20: 320–328.
2. Hazra TK, Das A, Das S, Choudhury S, Kow YW, et al. (2007) Oxidative DNA damage repair in mammalian cells: a new perspective. DNA Repair (Amst) 6: 470–480.
3. Kim HJ, Jee HJ, Yun J (2011) DNA damage induces down-regulation of PEPCK and G6P gene expression through degradation of PGC-1alpha. Acta Biochim Biophys Sin (Shanghai) 43: 589–594.
4. Sampath H, McCullough AK, Lloyd RS (2012) Regulation of DNA glycosylases and their role in limiting disease. Free Radic Res 46: 460–478.

5. Klungland A, Bjelland S (2007) Oxidative damage to purines in DNA: role of mammalian Ogg1. DNA Repair (Amst) 6: 481–488.
6. Klungland A, Rosewell I, Hollenbach S, Larsen E, Daly G, et al. (1999) Accumulation of premutagenic DNA lesions in mice defective in removal of oxidative base damage. Proc Natl Acad Sci U S A 96: 13300–13305.
7. Nishioka K, Ohtsubo T, Oda H, Fujiwara T, Kang D, et al. (1999) Expression and differential intracellular localization of two major forms of human 8-oxoguanine DNA glycosylase encoded by alternatively spliced OGG1 mRNAs. Mol Biol Cell 10: 1637–1652.
8. Radicella JP, Dherin C, Desmaze C, Fox MS, Boiteux S (1997) Cloning and characterization of hOGG1, a human homolog of the OGG1 gene of Saccharomyces cerevisiae. Proc Natl Acad Sci U S A 94: 8010–8015.
9. Rosenquist TA, Zharkov DO, Grollman AP (1997) Cloning and characterization of a mammalian 8-oxoguanine DNA glycosylase. Proc Natl Acad Sci U S A 94: 7429–7434.
10. Paz-Elizur T, Sevilya Z, Leitner-Dagan Y, Elinger D, Roisman LC, et al. (2008) DNA repair of oxidative DNA damage in human carcinogenesis: potential application for cancer risk assessment and prevention. Cancer Lett 266: 60–72.
11. Chevillard S, Radicella JP, Levalois C, Lebeau J, Poupon MF, et al. (1998) Mutations in OGG1, a gene involved in the repair of oxidative DNA damage, are found in human lung and kidney tumours [In Process Citation]. Oncogene 16: 3083–3086.
12. Lu R, Nash HM, Verdine GL (1997) A mammalian DNA repair enzyme that excises oxidatively damaged guanines maps to a locus frequently lost in lung cancer. Curr Biol 7: 397–407.
13. Michaels ML, Miller JH (1992) The GO system protects organisms from the mutagenic effect of the spontaneous lesion 8-hydroxyguanine (7,8-dihydro-8-oxoguanine). J Bacteriol 174: 6321–6325.
14. Okasaka T, Matsuo K, Suzuki T, Ito H, Hosono S, et al. (2009) hOGG1 Ser326Cys polymorphism and risk of lung cancer by histological type. J Hum Genet 54: 739–745.
15. Sakumi K, Tominaga Y, Furuichi M, Xu P, Tsuzuki T, et al. (2003) Ogg1 knockout-associated lung tumorigenesis and its suppression by Mth1 gene disruption. Cancer Res 63: 902–905.
16. Thomas D, Scot AD, Barbey R, Padula M, Boiteux S (1997) Inactivation of OGG1 increases the incidence of G. C–>T. A transversions in Saccharomyces cerevisiae: evidence for endogenous oxidative damage to DNA in eukaryotic cells. Mol Gen Genet 254: 171–178.
17. Fukae J, Takanashi M, Kubo S, Nishioka K, Nakabeppu Y, et al. (2005) Expression of 8-oxoguanine DNA glycosylase (OGG1) in Parkinson's disease and related neurodegenerative disorders. Acta Neuropathol 109: 256–262.
18. Nakabeppu Y, Tsuchimoto D, Yamaguchi H, Sakumi K (2007) Oxidative damage in nucleic acids and Parkinson's disease. J Neurosci Res 85: 919–934.
19. Cardozo-Pelaez F, Cox DP, Bolin C (2005) Lack of the DNA repair enzyme OGG1 sensitizes dopamine neurons to manganese toxicity during development. Gene Expr 12: 315–323.
20. Dezor M, Dorszewska J, Florczak J, Kempisty B, Jaroszewska-Kolecka J, et al. (2011) Expression of 8-oxoguanine DNA glycosylase 1 (OGG1) and the level of p53 and TNF-alphalpha proteins in peripheral lymphocytes of patients with Alzheimer's disease. Folia Neuropathol 49: 123–131.
21. Iida T, Furuta A, Nishioka K, Nakabeppu Y, Iwaki T (2002) Expression of 8-oxoguanine DNA glycosylase is reduced and associated with neurofibrillary tangles in Alzheimer's disease brain. Acta Neuropathol 103: 20–25.
22. Dorszewska J, Kempisty B, Jaroszewska-Kolecka J, Rozycka A, Florczak J, et al. (2009) Expression and polymorphisms of gene 8-oxoguanine glycosylase 1 and the level of oxidative DNA damage in peripheral blood lymphocytes of patients with Alzheimer's disease. DNA Cell Biol 28: 579–588.
23. Shao C, Xiong S, Li GM, Gu L, Mao G, et al. (2008) Altered 8-oxoguanine glycosylase in mild cognitive impairment and late-stage Alzheimer's disease brain. Free Radic Biol Med 45: 813–819.
24. Mao G, Pan X, Zhu BB, Zhang Y, Yuan F, et al. (2007) Identification and characterization of OGG1 mutations in patients with Alzheimer's disease. Nucleic Acids Res 35: 2759–2766.
25. Kaneko T, Tahara S, Matsuo M (1996) Non-linear accumulation of 8-hydroxy-2′-deoxyguanosine, a marker of oxidized DNA damage, during aging. Mutat Res 316: 277–285.
26. Radak Z, Boldogh I (2010) 8-Oxo-7,8-dihydroguanine: links to gene expression, aging, and defense against oxidative stress. Free Radic Biol Med 49: 587–596.
27. Radak Z, Bori Z, Koltai E, Fatouros IG, Jamurtas AZ, et al. (2011) Age-dependent changes in 8-oxoguanine-DNA glycosylase activity are modulated by adaptive responses to physical exercise in human skeletal muscle. Free Radic Biol Med 51: 417–423.
28. Radak Z, Naito H, Kaneko T, Tahara S, Nakamoto H, et al. (2002) Exercise training decreases DNA damage and increases DNA repair and resistance against oxidative stress of proteins in aged rat skeletal muscle. Pflugers Arch 445: 273–278.
29. Sampath H, Batra AK, Vartanian V, Carmical JR, Prusak D, et al. (2011) Variable penetrance of metabolic phenotypes and development of high-fat diet-induced adiposity in NEIL1-deficient mice. Am J Physiol Endocrinol Metab 300: E724–734.
30. Wood LJ, Nail LM, Perrin NA, Elsea CR, Fischer A, et al. (2006) The cancer chemotherapy drug etoposide (VP-16) induces proinflammatory cytokine production and sickness behavior-like symptoms in a mouse model of cancer chemotherapy-related symptoms. Biol Res Nurs 8: 157–169.
31. Arai T, Kelly VP, Minowa O, Noda T, Nishimura S (2006) The study using wild-type and Ogg1 knockout mice exposed to potassium bromate shows no tumor induction despite an extensive accumulation of 8-hydroxyguanine in kidney DNA. Toxicology 221: 179–186.
32. Burgess SC, Leone TC, Wende AR, Croce MA, Chen Z, et al. (2006) Diminished hepatic gluconeogenesis via defects in tricarboxylic acid cycle flux in peroxisome proliferator-activated receptor gamma coactivator-1alpha (PGC-1alpha)-deficient mice. J Biol Chem 281: 19000–19008.
33. Puigserver P (2005) Tissue-specific regulation of metabolic pathways through the transcriptional coactivator PGC1-alpha. Int J Obes (Lond) 29 Suppl 1: S5–9.
34. Liu C, Lin JD (2011) PGC-1 coactivators in the control of energy metabolism. Acta Biochim Biophys Sin (Shanghai) 43: 248–257.
35. Fernandez-Marcos PJ, Auwerx J (2011) Regulation of PGC-1alpha, a nodal regulator of mitochondrial biogenesis. Am J Clin Nutr 93: 884S–890.
36. Lin J, Yang R, Tarr PT, Wu PH, Handschin C, et al. (2005) Hyperlipidemic effects of dietary saturated fats mediated through PGC-1beta coactivation of SREBP. Cell 120: 261–273.
37. Sahin E, Colla S, Liesa M, Moslehi J, Muller FL, et al. (2011) Telomere dysfunction induces metabolic and mitochondrial compromise. Nature 470: 359–365.
38. Feilchenfeldt J, Brundler MA, Soravia C, Totsch M, Meier CA (2004) Peroxisome proliferator-activated receptors (PPARs) and associated transcription factors in colon cancer: reduced expression of PPARgamma-coactivator 1 (PGC-1). Cancer Lett 203: 25–33.
39. Watkins G, Douglas-Jones A, Mansel RE, Jiang WG (2004) The localisation and reduction of nuclear staining of PPARgamma and PGC-1 in human breast cancer. Oncol Rep 12: 483–488.
40. Jiang WG, Douglas-Jones A, Mansel RE (2003) Expression of peroxisome-proliferator activated receptor-gamma (PPARgamma) and the PPARgamma co-activator, PGC-1, in human breast cancer correlates with clinical outcomes. Int J Cancer 106: 752–757.
41. Thameem F, Puppala S, Lehman DM, Stern MP, Blangero J, et al. (2010) The Ser(326)Cys Polymorphism of 8-Oxoguanine Glycosylase 1 (OGG1) Is Associated with Type 2 Diabetes in Mexican Americans. Hum Hered 70: 97–101.
42. Daimon M, Oizumi T, Toriyama S, Karasawa S, Jimbu Y, et al. (2009) Association of the Ser326Cys polymorphism in the OGG1 gene with type 2 DM. Biochem Biophys Res Commun 386: 26–29.
43. Vartanian V, Lowell B, Minko IG, Wood TG, Ceci JD, et al. (2006) The metabolic syndrome resulting from a knockout of the NEIL1 DNA glycosylase. Proc Natl Acad Sci U S A 103: 1864–1869.
44. Torisu K, Tsuchimoto D, Ohnishi Y, Nakabeppu Y (2005) Hematopoietic tissue-specific expression of mouse Neil3 for endonuclease VIII-like protein. J Biochem 138: 763–772.
45. Li G, Yuan K, Yan C, Fox J 3rd, Gaid M, et al. (2011) 8-Oxoguanine-DNA glycosylase 1 deficiency modifies allergic airway inflammation by regulating STAT6 and IL-4 in cells and in mice. Free Radic Biol Med 52: 392–401.
46. Casorelli I, Pannellini T, De Luca G, Degan P, Chiera F, et al. (2010) The Mutyh base excision repair gene influences the inflammatory response in a mouse model of ulcerative colitis. PLoS One 5: e12070.

Published online 16 August 2012

Nucleic Acids Research, 2012, Vol. 40, No. 19 ***9717–9737***
doi:10.1093/nar/gks774

p32/gC1qR is indispensable for fetal development and mitochondrial translation: importance of its RNA-binding ability

Mikako Yagi[1], Takeshi Uchiumi[1,*], Shinya Takazaki[1], Bungo Okuno[1], Masatoshi Nomura[2], Shin-ichi Yoshida[3], Tomotake Kanki[1] and Dongchon Kang[1,*]

[1]Department of Clinical Chemistry and Laboratory Medicine, [2]Department of Medicine and Bioregulatory Science and [3]Department of Bacteriology, Graduate School of Medical Sciences, Kyushu University, 3-1-1 Maidashi, Higashi-ku, Fukuoka 812-8582, Japan

Received March 21, 2012; Revised July 23, 2012; Accepted July 24, 2012

ABSTRACT

p32 is an evolutionarily conserved and ubiquitously expressed multifunctional protein. Although p32 exists at diverse intra and extracellular sites, it is predominantly localized to the mitochondrial matrix near the nucleoid associated with mitochondrial transcription factor A. Nonetheless, its function in the matrix is poorly understood. Here, we determined p32 function via generation of p32-knockout mice. p32-deficient mice exhibited mid-gestation lethality associated with a severe developmental defect of the embryo. Primary embryonic fibroblasts isolated from p32-knockout embryos showed severe dysfunction of the mitochondrial respiratory chain, because of severely impaired mitochondrial protein synthesis. Recombinant p32 binds RNA, not DNA, and endogenous p32 interacts with all mitochondrial messenger RNA species *in vivo*. The RNA-binding ability of p32 is well correlated with the mitochondrial translation. Co-immunoprecipitation revealed the close association of p32 with the mitoribosome. We propose that p32 is required for functional mitoribosome formation to synthesize proteins within mitochondria.

INTRODUCTION

Mitochondria are essential organelles that are present in virtually all eukaryotic cells. The primary function of mitochondria is ATP production via the oxidative phosphorylation (OXPHOS) pathway. Additionally, mitochondria perform crucial roles in many other metabolic, regulatory and developmental processes. The circular 16.5-kb human mitochondrial DNA (mtDNA) molecule encodes 2 rRNAs, 22 tRNAs and 13 proteins that are members of the respiratory chain (1–3). All other proteins, including the mitochondrial translation apparatus, are derived from nuclear genes and are imported from the cytoplasm. In addition to core components of the small and large subunits of mitochondrial ribosomes (mitoribosomes), many other factors are required for translation initiation, elongation and termination in mitochondria (4).

Mammalian cells contain up to thousands of copies of mtDNA, which are organized in nucleoids (5,6). Mitochondrial transcription factor A (TFAM) is a key activator of mitochondrial transcription, and is a participant in mitochondrial genome replication to maintain mtDNA (7). It may also be a primary factor for packaging mtDNA in the nucleoid (8). Nucleoids may dynamically change their structure and distribution within mitochondria that are undergoing fission and fusion and are involved in various dynamic processes including mitochondrial replication, transcription and translation (9). Previously, we isolated p32 as a protein associated with TFAM (10).

Transcription from both the heavy-strand promoter (HSP) and light-strand promoter (LSP) generates polycistronic molecules that almost cover the entire H- and L-strand, respectively. It is generally accepted that tRNAs are excised from long polycistronic primary transcripts to generate mature messenger RNAs (mRNAs) and ribosomal RNAs (rRNAs); this is called the tRNA punctuation model (11–13). During or immediately after

*To whom correspondence should be addressed. Tel: +81 92 642 5750; Fax: +81 92 642 5772; Email: uchiumi@cclm.med.kyushu-u.ac.jp
Correspondence may also be addressed to Dongchon Kang. Tel: +81 92 642 5748; Fax: +81 92 642 5772; Email: kang@cclm.med.kyushu-u.ac.jp

The authors wish it to be known that, in their opinion, the first two authors should be regarded as joint First Authors.

cleavage of tRNAs, mRNAs are polyadenylated by a mitochondrial poly(A) polymerase. Indeed, in the case of some mRNAs, poly(A) tail addition is necessary to form a stop codon at the end of the open reading frame and may also be necessary for stabilization of some RNAs (14–16). Thus, nine monocistronic and two dicistronic mRNA transcripts are formed. Mitochondrial mRNAs do not contain 5′-modifications (13), and to date there has been no report of a canonical mitochondrial poly(A)-binding protein. Bioinformatic analyses revealed no obvious candidate, although several metabolic mitochondrial enzymes have been shown to be capable of binding RNA and poly(A) sequences (17,18). Another important post-transcriptional process is mRNA transfer to the mitoribosome, which is required to control RNA levels and translational activity. However, the proteins involved and the exact mechanism are yet to be revealed.

Protein–RNA interactions play essential roles in post-transcriptional control of gene expression including splicing, nuclear-cytoplasmic transport, localization, quality control, mRNA degradation and translational regulation (19). Numerous mitochondrial RNA-binding proteins without known RNA-binding domains have also been identified (18). AUH (AU RNA-binding protein /enoyl-CoA hydratase), which forms a doughnut-like structure composed of two trimers, is highly positively charged because of lysine residues in its α-helix H1 that is located on the edge of the cleft between the trimers. A mutational analysis showed that the lysine residues in the α-helix H1 are essential for the RNA-binding activity of AUH (20,21).

p32 [complement component 1, q subcomponent-binding protein (C1qBP); also called gC1qR or HABP1] was first isolated from a membrane preparation of Raji cells and originally copurified with the pre-mRNA splicing factor SRSF1 (also called SF2 and ASF) in human HeLa cells (22). The p32 protein is a doughnut-shaped trimer, which primarily localizes to the mitochondrial matrix, but has also been reported to be present at the cell surface, in the nucleus and cytosol, as well as within secretory granules (23–26). p32 is synthesized as a pre protein and is processed by proteolytic cleavage of the N-terminal amino acids containing the mitochondrial signal sequence (27). The pre-protein form of p32 is only expressed in germ cells (28), which clearly justifies the predominant localization of p32 in the mitochondrial matrix.

Human p32 interacts with various molecules including hyaluronic acids, human immunodeficiency virus Tat protein, complement 1q, proapoptotic factor HRK and tumor suppressor ARF (29–31). These observations suggest that p32 may be a multifunctional chaperone protein (32). HABP1/p32/C1qBP represented as, synonym in Human Genome, exhibits structural plasticity influenced by ionic environment due to asymmetric charge distribution. The presence of salt stabilizes the compact trimeric conformation and can interact with hyaluronan only (33). Thus, one of the ligand of this protein is hyaluronan, a complex mucopolysaccharide which is well known for its regulatory role during embryonic development (34). p32/HABP1 expression in *Schizosaccharomyces pombe* induces growth inhibition and morphological abnormalities such as elongation, multinucleation and aberrant cell septum formation in several strains, implying a role for this protein in cell-cycle progression and cytokinesis (35). However, the primary physiological role of p32 in mammalian cells is unclear, particularly in the mitochondrial matrix, despite its predominant localization there.

Previously, we identified a *Saccharomyces cerevisiae* homolog of human p32, mam33, which localized to the mitochondrial matrix. Mam33-deficient yeast cells are significantly defective in maintenance of the mitochondrial genome and show impairment of mitochondrial ATP synthesis. The growth impairment is restored by the introduction of human *p32* cDNA, which demonstrates the evolutionarily conserved function of p32 homologs among eukaryotes. Taken together, we propose that both human p32 and yeast mam33 reside in the mitochondrial matrix and play an important role in maintaining mitochondrial OXPHOS (27). Very recently, p32-knockdown cells exhibited reduced synthesis of mtDNA-encoded OXPHOS polypeptides and were less tumorigenic *in vivo* (36).

To explore the role of the p32 protein *in vivo*, particularly in the mitochondrial matrix, we generated mice with a homozygous disruption of the *p32* gene. We show that p32 inactivation causes mid-gestation lethality of knockout embryos and defects in OXPHOS, because of severe impaired protein synthesis of mtDNA-encoded protein. Here, we propose that the mitochondrial matrix protein p32 functions as an essential RNA-binding factor in mitochondrial translation, and is indispensable for embryonic development.

MATERIALS AND METHODS

Animals

Animals were mated overnight, and females were examined for a vaginal plug the following morning. At noon of that day, vaginal plug detection was recorded as embryonic day (E) 0.5. Mouse experiments were performed in accordance with the guidelines of the animal ethics committee of Kyushu University Graduate School of Medicine, Japan.

Immunoblotting

Briefly, cells were lysed with lysis buffer (50 mM Tris–HCl, pH 7.5, 1 mM EDTA, 150 mM NaCl and 0.5% NP-40) and then subjected to immunoblotting as described elsewhere (37). Signals were visualized with horseradish peroxidase (HRP)-conjugated anti-rabbit IgG and an enhanced chemiluminescence reagent (GE Healthcare, Piscataway, NJ). Chemiluminescence was recorded and quantified with a chilled charge-coupled device camera (LAS1000plus).

Immunofluorescence imaging of mouse embryonic fibroblasts

Immunofluorescence was carried out according to established techniques. Briefly, mouse embryonic fibroblasts

(MEFs) were incubated in the presence of 500 nM MitoTracker Red (Invitrogen) for 20 min. Cells were fixed and permeabilized, then incubated with a 1:200 dilution of anti-p32 serum in PBS/1% bovine serum albumin (BSA) for 1 h. Glass slides were mounted using Superfrost (Matsunami). Fluorescence images were obtained using a confocal laser microscope (Nikon).

Antibodies

Polyclonal antibodies against mouse p32, HA, TFAM, LRPPRC and VDAC were raised in our laboratory. Antibodies against COXI, COXIII, NDUFA9, SDHA, UQCRFS1, ATP synthase and COXVa were purchased from Invitrogen. Antibodies against β-actin, MRPS22, MRPS29 and MRPL3 were purchased from Sigma, Proteintech Group Inc, BD Biosciences and Abcam, respectively. Alexa 488-conjugated anti-rabbit and anti-mouse IgG for fluorescence microscopy, Alexa 568-conjugated anti-mouse IgG for fluorescence microscopy of paraffin-embedded tissue sections, HRP-conjugated anti-mouse IgG and diaminobenzidine (DAB) for BrdU staining were all purchased from Nichirei.

MEF culture and cell proliferation assay

SV40 large T antigen-immortalized MEFs were generated from E14 p32flox/flox C57BL/6 embryos by standard methods. MEFs and HeLa cell were cultured in Dulbecco's modified Eagle's medium (DMEM) (1000 mg/l glucose) supplemented with 10% FBS at 37°C in a humidified atmosphere with 5% CO_2. For cell proliferation assay, MEF cells (1×10^4) were seeded in triplicate in 35 mm dishes and cultured in DMEM (1000 mg/l glucose) plus dialyzed 10% fetal bovine serum (FBS) without pyruvate. Cells were trypsinized and counted daily for up to 96 h using a Coulter Counter (Beckman Coulter). Pyruvate (1 mM), uridine (0.2 mM) and glucose (3500 mg/l) were added on Days 0 and 4. We used dialyzed FBS to remove small molecules such as uridine and pyruvate.

RNA band-shift assays

RNA electrophoretic mobility shift assays (REMSAs) were carried out according to established techniques. Briefly, a synthesized oligonucleotide probe (DNA or RNA) was end-labeling in the presence of [γ-^{32}P]ATP by a T4 polynucleotide kinase. To form RNA–protein complexes, the indicated amount of purified His-p32 was incubated with the ^{32}P-labeled oligonucleotide probe at 25°C for 30 min in binding buffer [10 mM HEPES, pH 7.6, 3 mM $MgCl_2$, 20 mM KCl, 1 mM dithiothreitol (DTT), 50 U RNase inhibitor (Toyobo) and 5% glycerol]. Heparin (5 μg) was added for a further 10 min incubation to prevent non-specific binding. Samples were electrophoresed in a 6% non-denaturing polyacrylamide gel in Tris–borate buffer. Gels were dried and visualized using a BAS2500 (Fuji).

Sucrose gradient analysis of mitochondrial ribosomes

MEFs were solubilized in a non-ionic detergent (1% lauryl maltoside). Total cell lysates (2 mg) were loaded onto a 15–30% sucrose density gradient in 20 mM Tris–HCl, pH 7.5, 150 mM NaCl and 1 mM $CaCl_2$, and then centrifuged at 100 000*g* for 3 h at 4°C in a swinging bucket rotor (SW 40.1; Beckman Coulter). After separation, 17 fractions were precipitated by 10% trichloroacetic acid and washed in acetone, and then the entire fraction was resolved by SDS–polyacrylamide gel electrophoresis (PAGE).

ATP quantification

Cellular ATP was quantified using an ATP-determination kit according to the manufacturer's instructions (Promega). Briefly, four MEFs, plated at equal densities, were lysed in passive lysis buffer (Promega). Equal volumes of cell lysate were added to the standard reaction solution, and luminescence was measured and normalized to the protein amount in each lysate. The values used were in the linear range of the assay as determined by a standard curve.

Oxygen consumption assay

Oxygen consumption was measured as described elsewhere (38). MEFs were trypsinized, PBS washed twice and then permeabilized with 0.1 μg/ml digitonin. The optimum incubation time for permeabilization (50 s for MEFs) was determined for each cell line as the shortest time after which 99% of cells were trypan blue-positive. Cells were placed into the reaction chamber of a Clark-type electrode (Hansatech), and oxygen concentrations were measured in 1 ml volumes at 37°C with substrates (glutamate + malate, succinate + glycerol-3-phosphate; Sigma) and inhibitors according to standard protocols (39). Oxygen consumption was represented as the mean ± SD, nanomoles O_2 consumed per minute per cell.

Expression constructs

The expression construct containing mouse p32 cDNA was generated by standard methods. Site-directed mutagenesis to generate p32 mutants K89A and K93A was performed using methods described elsewhere (37). cDNAs of wild-type and mutant K89A/K93A p32 were cloned into the BamHI/XhoI sites of the expression vector pcDNA3 (Invitrogen).

Immunoprecipitation using anti-HA antibodies

Immunoprecipitation (IP) was carried out according to established techniques (37). Doxycycline-induced and non-induced HeLa (p32-HA) cells (1×10^8 cells) and MEF cells were homogenized and centrifuged at 900*g* for 10 min. The supernatant (adjusted to 10% Percoll) was overlaid on a discontinuous Percoll density gradient (4 ml of 40% and 4 ml of 20% Percoll buffer; GE Healthcare) in a 12 ml centrifugation tube. After centrifugation at 60 000*g* for 1 h using a SW41-Ti rotor (Beckman Coulter), the mitochondrial phase located in the middle of the tube was collected. Two to three milligrams of

mitochondrial protein were solubilized in 1 ml IP buffer (10 mM Tris–HCl, pH 7.4, 150 mM NaCl, 1 mM EDTA, 1% NP-40 and 0.1% SDS) containing 40 µl of beads coated with anti-HA or anti-p32 antibody. After 12 h of rotation, the beads were washed four times with IP buffer and eluted with 0.1 M glycine (pH 2.5).

Pulse-labeling of mitochondrial translation products

Mitochondrial translation products were pulse-labeled *in vitro* with [^{35}S]-(methionine and cysteine) (GE Healthcare). In experiments where the label was chased, cells were incubated for 6 min in 100 µg/ml emetine or 250 µg/ml chloramphenicol prior to labeling for 60 min. Labeled cells were then rinsed with an Hypotonic buffer (10 mM Tris–HCl, pH 7.4, 150 mM $MgCl_2$, 10 mM KCl). After centrifugation at 1150*g* for 5 min, cell pellets were resuspended in loading buffer consisting of 93 mM Tris–HCl, pH 6.7, 7.5% glycerol, 1% SDS, 0.25 mg/ml bromophenol blue and 3% mercaptoethanol. The total lysate was then subjected to 15% SDS-PAGE for 3 h at 180 V. Gels were measured using a BAS2500 (Fuji).

RNA co-IP with p32-HA protein

Briefly, HeLa whole cell lysates induced by doxycycline were first precleared with 50 µg rabbit IgG (Bio-Rad) for 15 min at 4°C, followed by binding to anti-HA-coated agarose beads or anti-LRPPRC antibody with protein G agarose for 12 h at 4°C. Then, p32-HA was eluted using glycine (pH 2.5), and RNA was extracted with an RNAeasy kit (Qiagen). The eluted RNA was treated with 100 U DNase I at 37°C for 20 min, and then the RNA was purified again with an RNAeasy kit.

Activity of respiratory mitochondrial complex

MEFs were lysed in a hypotonic buffer (2.5 mM Tris–HCl, pH 7.5 and 2.5 mM $MgCl_2$) on ice for 15 min, and then sonicated for 15 s (25% output, duty cycle; TAITEC) to measure respiratory complex activity.

To detect complex I activity, spectrophotometric assays were performed to evaluate NADH:Q oxidoreductase activity at 30°C by monitoring the decrease in the absorbance of nicotinamide adenine dinucleotide reduced form (NADH) at 340 nm, as described elsewhere (40). Briefly, 10 µM decylubiquinone (artificial electron acceptor), 2 µg antimycin A (complex III inhibitor), 5 mM sodium azide (NaN_3) (complex IV inhibitor) and 0.5 mg whole-cell lysate were mixed in 1 ml standard reaction medium (2.5 mM $MgCl_2$ and 50 mM inorganic phosphate, pH 7.3). The reaction was initiated with 100 µM NADH. The activity of the enzyme was determined by the difference of absorbance with and without 1.25 µg rotenone (complex I inhibitor). Data were expressed as nmol NADH oxidized/min/µg protein.

Succinate dehydrogenase (complex II) activity was determined spectrophotometrically at 30°C (41). Briefly, the reaction was initiated with 50 µM dichlorophenolindophenol (DCPIP; used as an artificial electron acceptor) in 1 ml standard reaction medium supplemented with 20 mM succinate, 2 µg rotenone, 2 µg antimycin A, 5 mM NaN_3 and 0.1 mg whole-cell lysate.

Cytochrome c reductase (complex III) activity was evaluated spectrophotometrically at 30°C by monitoring the increase in absorbance at 550 nm of cytochrome c. Briefly, the reaction was initiated by the addition of 5 mM reduced decylubiquinone to 1 ml standard reaction medium supplemented with 2 µg rotenone, 5 mM NaN, 60 µM cytochrome c and cell lysate. The reaction was stopped by addition of 2 µg Antimycin A.

Cytochrome c oxidase (complex IV) activity was determined spectrophotometrically at 550 nm at 30°C (42). Briefly, the reaction was initiated by the addition of 50 µg whole-cell lysate to 1 ml standard reaction medium supplemented with 20 µM ferrocytochrome c.

mRNA quantification

RT of 1 µg total RNA was performed with random hexamer primers using SuperScript II RT (Invitrogen) according to the manufacturer's instructions. The expression of mitochondrial genes was detected by qPCR with a thermal cycler (StepOne plus; Applied Biosystems). PCR primers are listed in Supplementary Table S1.

Measurement of mitochondrial membrane potential

Mitochondrial membrane potential ($\Delta\psi$m) was estimated using a JC-1 probe (Invitrogen). This reagent is a highly reliable, cationic and mitochondria-specific fluorescent dye, which becomes concentrated in mitochondria in proportion to the membrane potential, because it is highly lipophilic. Increasing amounts of dye accumulate in mitochondria with increasing $\Delta\psi$m and ATP-generating capacity. The dye is present as monomers at lower concentrations (green fluorescence), but at higher concentrations forms J-aggregates (red fluorescence). The ratio of the fluorescence at 590 nm to that at 527 nm represents the relative $\Delta\psi$m value. Fluorescence was measured at the two wavelengths by a FACS Caliber (Becton Dickinson).

RESULTS

Disruption of *p32* causes embryonic lethality

To experimentally address the function of p32 in a physiological *in vivo* context, we used gene targeting to generate p32-deficient mice. We constructed a gene replacement vector that introduced a gene cassette, consisting of the neomycin resistance gene (*Neo*) and flanking *loxP* sites upstream and downstream of exon 3, into the endogenous *p32* gene (Supplementary Figure S1A). After injection of embryonic stem cells harboring the targeted allele, germline transmission was confirmed by Southern blotting and PCR analysis (Supplementary Figure S1B and S1C). Heterozygous $p32^{+/-}$ mice were generated by breeding $p32^{fl/+}$ mice with a *Cre* transgenic mouse strain (EII-Cre) allowing universal expression of Cre-recombinase in all tissues. Intercrosses of $p32^{+/-}$ mice revealed no viable $p32^{-/-}$ offspring (Supplementary Figure S1D and Table 1). To determine the time at which the p32 mutant became lethal, we examined embryos from $p32^{+/-}$ intercrosses at various developmental stages. In contrast to wild-type embryos, the growth of

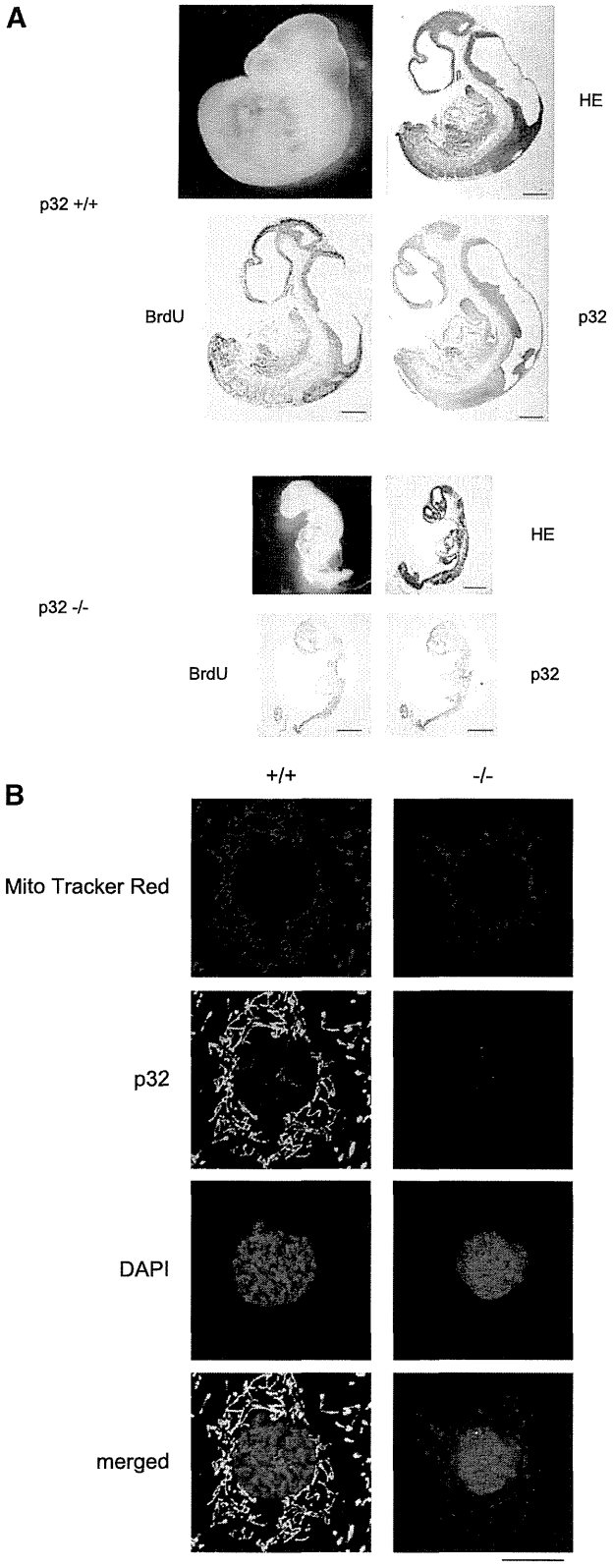

Figure 1. Disruption of p32 causes embryonic lethality. (**A**) Whole mounts of E10.5 $p32^{-/-}$ embryos and histological analysis of $p32^{-/-}$ embryos compared with those of wild-type $p32^{+/+}$ littermates. Photomicrographs (upper left) and hematoxylin and eosin (HE) staining (upper right) are shown. Pregnant mice were injected with BrdU at 2 h prior to dissection. Sections of $p32^{+/+}$ and $p32^{-/-}$ embryos at E10.5 were stained with BrdU (lower left) or an anti-p32 antibody (lower right). *In vivo* labeling with BrdU revealed arrest of proliferation in E10.5 embryos. Scale bars: 500 μm. (**B**) Immunofluorescence staining of p32 and MitoTracker Red in wild-type and p32-knockout cells. Nuclei were stained with 4′,6-diamidino-2-phenylindole (DAPI). MEFs were treated with MitoTracker Red (500 nM) for 20 min before p32 staining. Cells were fixed, fluorescently stained by anti-p32 antibodies, and then analyzed by confocal microscopy. The lower panel shows merged images. Scale bar: 20 μm.

Table 1. p32 deficiency causes embryonic lethality

	Genotype			Disintegrated or resorbed	Total
	+/+	+/−	−/−		
E8.5	8	19	5	5	32
E9.5	17	35	15	17	67
E10.5	5	16	7	10	28
E11.5	4	15	6	4	25
E12.5	1	9	2	3	12
E13.5	3	21	1	2	25
Newborn	21	41	0		62

Embryos at the indicated stages were isolated from intercrosses of heterozygous mice, and the total numbers (*n*) of intact and disintegrated or resorbed embryos were counted.

$p32^{-/-}$ embryos appeared retarded as early as E10.5. Most $p32^{-/-}$ embryos had been resorbed by E11.5, and therefore $p32^{-/-}$ embryos died between E10.5 and E11.5.

The phenotype of $p32^{-/-}$ embryos included markedly shrunken, poorly developed, pale and anemic organs (Figure 1A). p32 protein was absent from $p32^{-/-}$ embryos. In E10.5 $p32^{-/-}$ embryos, BrdU incorporation revealed that cells did not proliferate in various tissues including the brain, heart and liver. These data suggest that growth retardation, smaller size of organ and severe anemia account for the embryonic lethality of the p32 mutation.

Establishment of p32-knockout MEFs

To define the functional consequences of *p32* deletion, MEFs were isolated from homozygous $p32^{flox/flox}$ embryos and infected with a adenovirus encoding Cre-recombinase, which led to efficient deletion of p32 *in vitro*. We also immortalized $p32^{-/-}$ cells by transfection with a plasmid vector encoding the SV40 large T antigen. Western blot analysis confirmed the absence of p32 in $p32^{-/-}$ cells and half wild-type p32 levels in $p32^{+/-}$ cells (Supplementary Figure S2). $p32^{-/-}$ MEFs exhibited an enlarged and flattened cell morphology compared with that of $p32^{+/+}$ MEFs, suggesting that loss of p32-induced cell morphological change.

Abnormal mitochondrial morphology in $p32^{-/-}$ MEFs

Maintenance of proper mitochondrial morphology is critical for the function of this organelle. The basic morphology of mitochondria in cells is a dynamic tubulovesicular reticulum. Mitochondrial morphology changes dynamically as a result of a balance in the fusion and fission occurring in response to cellular energy demands, differentiation and pathological conditions (43,44). Therefore, we determined the effect of p32 depletion on the morphology of mitochondria using

Mitotracker Red in $p32^{+/+}$ and $p32^{-/-}$ MEF cell lines. In wild-type cells, p32 colocalized to the tubulovesicular mitochondria. In contrast, upon loss of p32, the tubular mitochondrial organization shifted to a punctate, granular shape (Figure 1B). This result suggests that the loss of p32 exhibited tubulovesicular morphological change.

Establishment of mitochondrial re-expression of p32

To directly confirm that p32 regulated mitochondrial function, we expressed mitochondria-targeted and cytoplasmic forms of p32 in $p32^{-/-}$ MEFs. We obtained stable $p32^{-/-}$ MEFs that expressed a low level of mitochondrially targeted p32 (immature) (Supplementary Figure S3A). The recombinant p32 was the same size as endogenous p32, suggesting that we successfully restored p32 expression in knockout cells, albeit at low levels. The cDNA construct encoded a p32 protein lacking the first 71 amino acids, which produced a cytoplasm-only p32. The expression level of this cytoplasm-only p32 was significantly lower than that of the mitochondria-targeted p32 (Supplementary Figure S3B). We were able to observe the cytoplasmic p32 only after inhibition of proteasomal degradation with MG-132 (Supplementary Figure S3C). These data suggest that cytoplasmic p32, which is unable to localize to the mitochondria, is extremely unstable in MEFs.

Loss of p32 reduced complex activity

We first sought to investigate a possible role for p32 in OXPHOS. The electron transport chain consists of five multi-subunit enzymatic complexes formed from the products of both nuclear and mitochondrial genes. We measured the activities of the electron transport chain complexes by spectroscopic assays that revealed the activities of complexes I, III and IV were strongly reduced in $p32^{-/-}$ cells, while the activity of complex II was unchanged (Figure 2A). Interestingly, complex II is the only OXPHOS complex encoded exclusively by nuclear DNA. Re-expression of p32 in $p32^{-/-}$ cells partially restored complex I, III and IV activities. These finding suggested that p32 might be involved in mtDNA-related protein function because complexes I, III and IV include proteins encoded by mtDNA.

Mammalian p32 is required for oxidative respiration

To further test mitochondrial OXPHOS function, we measured cellular respiration by polarographic assays of digitonin-permeabilized cells. Oxygen electrode studies showed a 3-fold decrease in oxygen consumption dependent on complexes I + III + IV (glutamate + malate) and complexes III + IV (succinate + G3P) in p32-knockout MEFs compared with those of wild-type MEFs (Figure 2B), indicating that p32 is required for mitochondrial respiration. Decreased respiration in p32-knockout MEFs suggests a reduction in functional respiratory complexes.

p32-knockout MEFs show reduced mitochondrial membrane potential and ATP production

We suspected that p32-mediated inhibition of the mitochondrial respiratory chain may affect the mitochondrial membrane potential ($\Delta\psi m$). The $\Delta\psi m$ value was measured using JC-1, a fluorescent dye sensitive to mitochondrial membrane potential. The $\Delta\psi m$ values of p32-knockout MEFs were lower than those of wild-type MEFs (Figure 2C). Carbonyl cyanide 3-chlorophenylhydrazone (CCCP)-treated cells served as a positive control for depolarization of the mitochondrial membrane.

Because mitochondria are the cellular powerhouses for energy production, we measured ATP levels in wild-type and $p32^{-/-}$ MEFs. In wild-type cells, the inhibition of glycolysis by 2-deoxy-glucose (2DG) only slightly decreased the ATP level (Figure 2D, upper set, $p32^{+/+}$, lane 2) probably because pyruvate in DMEM supported mitochondrial OXPHOS. After oligomycin, an inhibitor of complex V, was added together with 2DG, the cellular ATP level was strongly decreased (Figure 2D, upper set, $p32^{+/+}$, lane 3), indicating that wild-type MEFs were largely dependent on mitochondrial ATP production (see lower set and legends for calculation). The total ATP level was rather higher in p32-knockout MEFs than in wild-type MEFs (Figure 2D, upper set, $p32^{+/+}$, lane 1 and $p32^{-/-}$, lane 1). A marked decrease in mitochondrial ATP production by 2DG was observed in the knockout MEFs (upper set, $p32^{-/-}$, lane 2) and further addition of oligomycin marginally decreased the ATP production (upper set, $p32^{-/-}$, lane 3), indicating that p32-knockout MEFs mostly depends on glycolytic ATP production. The decrease in mitochondrial ATP production may be over-compensated by glycolytic ATP production that was estimated by 2DG-sensitive cellular ATP (Figure 2D, lower set table). Re-expression of p32 in $p32^{-/-}$ cells restored mitochondrial ATP production, but not the introduction of an empty vector, indicating that p32 is required for efficient ATP production via OXPHOS.

Retarded proliferation of $p32^{-/-}$ MEFs

To assess potential defects in proliferation caused by mitochondrial OXPHOS dysfunction, we cultured cells at a standard concentration of glucose (1000 mg/l) without pyruvate, which allowed easier observation of the effects of glucose on OXPHOS. We dialyzed FBS to remove small molecules such as uridine and pyruvate. As shown in Figure 2E, proliferation of p32-knockout MEFs was strongly retarded compared with that of wild-type cells. Re-expression of p32 in $p32^{-/-}$ MEFs rescued the growth retardation, indicating that p32 is important for normal cell proliferation.

Cells depleted of mtDNA would require high glucose, pyruvate and uridine for proliferation. To determine whether the addition of high glucose, pyruvate or uridine could rescue the proliferation of $p32^{-/-}$ MEFs, we added each of these supplements separately. Only pyruvate (1 mM) was able to rescue the proliferation of $p32^{-/-}$ MEFs (Figure 2E, lower panel); addition of high glucose (3500 mg/l) and uridine (0.2 mM) did not rescue

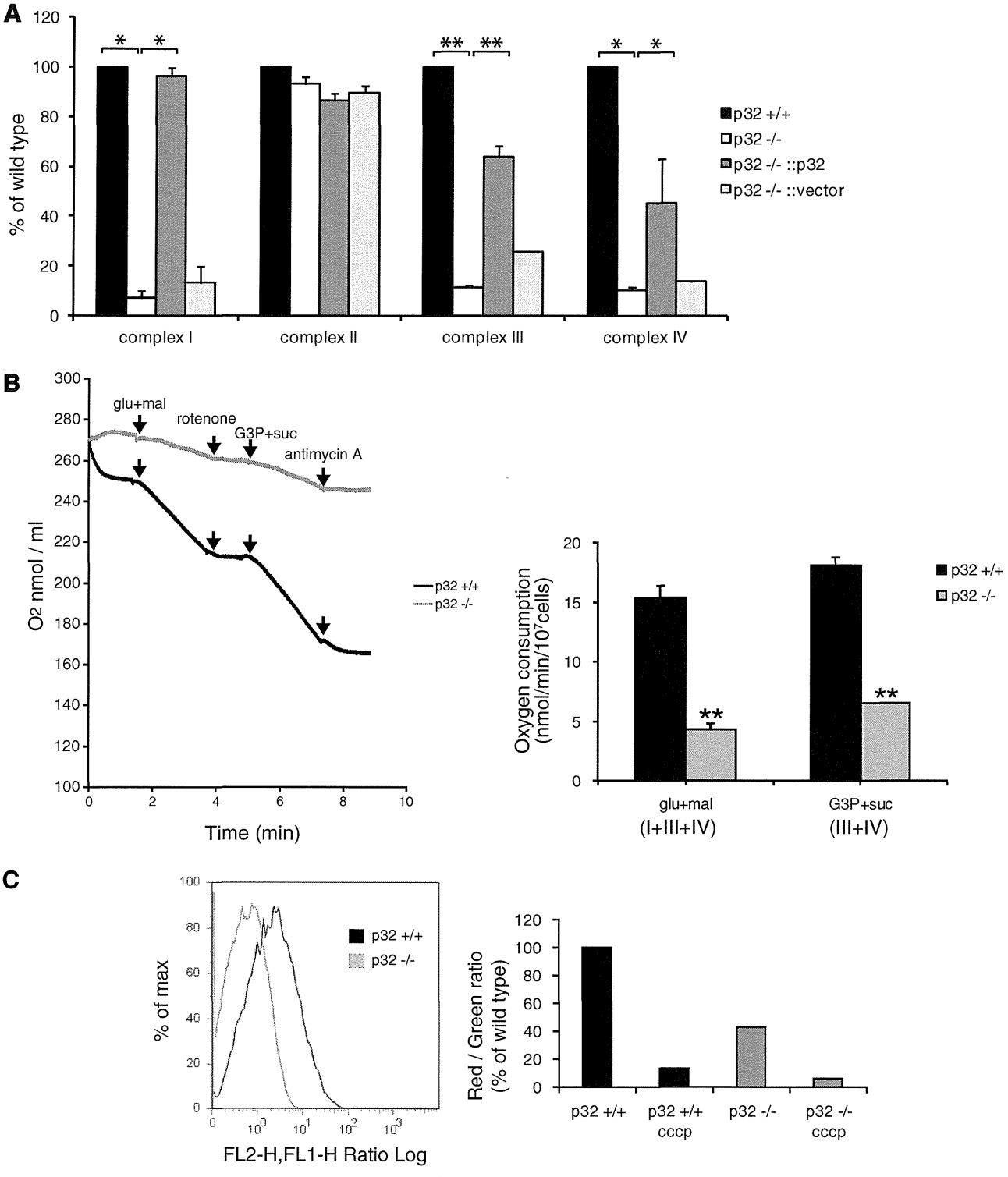

Figure 2. Reduced mitochondrial respiratory activities in $p32^{-/-}$ MEFs. (**A**) The activity of each complex was measured using cell lysates as described in 'Materials and Methods' section. Reduced enzymatic activities of mitochondrial complexes I, III and IV in p32-knockout cells were observed. In contrast, complex II activity was not decreased. Re-expression of p32 in $p32^{-/-}$ cells restored the enzymatic activities of complexes I, III and IV. The results represent the mean ± SD of three independent experiments. $*P < 0.05$; $**P < 0.01$ versus controls ($p32^{+/+}$ versus $p32^{-/-}$ and $p32^{-/-}$ versus $p32^{-/-}$::p32). (**B**) Oxygen consumption by digitonin-permeabilized wild-type ($p32^{+/+}$) and knockout ($p32^{-/-}$) MEFs. Glutamate and malate (glu+mal) respiration depends on the activities of complexes I, III and IV; glycerol-3-phosphate and succinate (G3P+suc) respiration depends on the activities of complexes III and IV. Rotenone (a complex I inhibitor) and Antimycin A (a complex III inhibitor) completely inhibit O_2 consumption at each step. Data show the mean ± SD of triplicate experiments and $**P < 0.01$ versus controls ($p32^{+/+}$ versus $p32^{-/-}$). (**C**) Decreased mitochondrial membrane potential in p32-knockout MEFs. MEFs were stained with the fluorescent dye JC-1 and then analyzed by flow cytometry at 527 and 590 nm. The fluorescence ratio of JC1 dimer (Red)/JC-1 monomer (Green) is shown. Dissipation of the membrane potential with CCCP was used as a control.

(continued)